

THE X-RAY SPECTRAL EVOLUTION OF GALACTIC BLACK HOLE X-RAY BINARIES TOWARD QUIESCENCE

RICHARD. M. PLOTKIN¹, ELENA GALLO¹, AND PETER G. JONKER^{2,3,4}

¹ Department of Astronomy, University of Michigan, 500 Church Street, Ann Arbor, MI 48109, USA; rplotkin@umich.edu

² SRON, Netherlands Institute for Space Research, Sorbonnelaan 2, 3584 CA, Utrecht, The Netherlands

³ Harvard-Smithsonian Center for Astrophysics, 60 Garden Street, Cambridge, MA 02138, USA

⁴ Department of Astrophysics/IMAPP, Radboud University Nijmegen, P.O. Box 9010, 6500 GL, Nijmegen, The Netherlands

Received 2013 February 27; accepted 2013 June 17; published 2013 July 25

ABSTRACT

Most transient black hole X-ray binaries (BHXBs) spend the bulk of their time in a quiescent state, where they accrete matter from their companion star at highly sub-Eddington luminosities (we define quiescence here as a normalized Eddington ratio $l_x = L_{0.5-10\text{ keV}}/L_{\text{Edd}} < 10^{-5}$). Here, we present *Chandra* X-ray imaging spectroscopy for three BHXB systems (H 1743–322, MAXI J1659–152, and XTE J1752–223) as they fade into quiescence following an outburst. Multiple X-ray observations were taken within one month of each other, allowing us to track each individual system’s X-ray spectral evolution during its decay. We compare these three systems to other BHXB systems. We confirm that quiescent BHXBs have softer X-ray spectra than low-hard-state BHXBs, and that quiescent BHXB spectral properties show no dependence on the binary system’s orbital parameters. However, the observed anti-correlation between X-ray photon index (Γ) and l_x in the low-hard state does not continue once a BHXB enters quiescence. Instead, Γ plateaus to an average $\langle \Gamma \rangle = 2.08 \pm 0.07$ by the time l_x reaches $\sim 10^{-5}$. $l_x \sim 10^{-5}$ is thus an observationally motivated upper limit for the beginning of the quiescent spectral state. Our results are discussed in the context of different accretion flow models and across the black hole mass scale.

Key words: accretion, accretion disks – black hole physics – X-rays: binaries

Online-only material: color figures

1. INTRODUCTION

Black holes are common in the universe, with a supermassive black hole likely at the center of every large galaxy (e.g., Kormendy & Richstone 1995; Marconi et al. 2004), and predictions of upward of 10^8 – 10^9 stellar mass black holes in the Milky Way alone (e.g., Shapiro & Teukolsky 1983; Maccarone 2005; Fender et al. 2013). Yet we can ultimately observe just a small fraction of these black holes, and it is only for an even smaller subset that we can appeal to dynamical interactions to infer their properties. We are forced to study the vast majority of known black holes through indirect methods, like the radiative signatures produced when they accrete matter. There is thus strong motivation to better understand accretion onto black holes. Studying accreting black holes not only provides direct constraints on Galactic black hole X-ray binaries (BHXBs), active galactic nuclei (AGNs), and black hole feedback, but also broad insight into many other classes of objects where similar physics is at play (e.g., young stars, white dwarfs, neutron stars, and gamma-ray bursts; see, e.g., Meier et al. 2001; Migliari & Fender 2006; K rding et al. 2008; Scaringi et al. 2012).

X-ray emission is a universal, but not yet fully understood, feature of accreting black holes. Complicating matters is that the most important physical mechanism(s) responsible for X-ray emission seems to depend largely (albeit not entirely) on the normalized mass accretion rate $\dot{m} \equiv \dot{M}/\dot{M}_{\text{Edd}}$ (e.g., Esin et al. 1997; Trump et al. 2011), where \dot{M} is the mass accretion rate in physical units (g s^{-1}) and \dot{M}_{Edd} is the Eddington mass accretion limit. Throughout this paper, we use the normalized Eddington X-ray luminosity ($l_x = L_X/L_{\text{Edd}}$, where L_X is the X-ray luminosity from 0.5 to 10 keV and $L_{\text{Edd}} = 1.26 \times 10^{38} [M/M_\odot] \text{ erg s}^{-1}$ for ionized hydrogen) as a proxy for \dot{m} . We note that l_x and \dot{m} correlate with each other, but in general

$l_x \neq \dot{m}$. Very low \dot{m} represents a particularly important regime. Most transient BHXBs spend the bulk of their time in a very weakly accreting quiescent state. While there is no standard definition for quiescence, a commonly used criterion is $L_X \sim 10^{30.5-10^{33.5}} \text{ erg s}^{-1}$ (corresponding to $l_x \sim 10^{-8.5-10^{-5.5}}$ for a $10 M_\odot$ black hole; Remillard & McClintock 2006). Most supermassive black holes in the local universe also accrete just as weakly. Yet we still need a better understanding of how quiescent black holes produce high-energy radiation, and of the structure and geometry of their accretion flows.

When a power law is fit to the X-ray spectra of black holes with $l_x \lesssim 10^{-2}$, an anti-correlation is seen between l_x and the photon power-law index Γ (e.g., Yuan et al. 2007; Wu & Gu 2008; Constantin et al. 2009; Gu & Cao 2009; Sobolewska et al. 2011; Younes et al. 2011; G ltekin et al. 2012). That is, lower accretion rate black holes have softer (i.e., steeper) X-ray spectra.⁶ However, this anti-correlation has not yet been fully probed below $l_x \sim 10^{-4}$. Exploring the Γ – l_x anti-correlation down to lower l_x will lead to a better understanding of the properties of black hole accretion flows in quiescence. Whether the X-ray spectral softening continues at all l_x or eventually saturates, and also if the softening is gradual or abrupt, can provide constraints on accretion disk/jet models (e.g., Tomsick et al. 2001). Furthermore, characterizing the behavior of Γ at very low l_x may allow for a more systematically determined definition of the quiescent state.

⁵ The X-ray photon index Γ is defined as $N(E) = N_0(E/E_0)^{-\Gamma}$, where $N(E)$ is the number of photons at a given energy E , N_0 is the photon number normalization, and E_0 is the reference energy (we set E_0 to 1 keV here).

⁶ This Γ – l_x anti-correlation is opposite to the trend observed at higher accretion rates for both BHXBs and for luminous quasars (e.g., Kubota & Makishima 2004; Shemmer et al. 2008; Grupe et al. 2010).

In this paper, we consider observations of BHXBs in order to help constrain this relatively unexplored very low l_x parameter space ($l_x \lesssim 10^{-4}$). Transient BHXBs undergo outbursts in luminosity that are marked by X-ray spectral state transitions accompanied by characteristic variability properties, as well as outflows in the forms of jets and/or winds (Remillard & McClintock 2006, also see, e.g., Fender et al. 2004, 2005, 2009; Belloni et al. 2005; Homan & Belloni 2005, for reviews on outburst phenomenology). Here, we consider only the final parts of BHXB outbursts, after a BHXB transitions back into a hard X-ray state (with $\Gamma \sim 1.5$; i.e., the “low–hard” state) and then decays into quiescence. So far, around a dozen BHXBs have been observed in quiescence with high enough sensitivity to extract X-ray spectral information. These quiescent BHXBs tend to be relatively soft with $\Gamma \sim 2$ (e.g., Ebisawa et al. 1994; Tomsick et al. 2004; Corbel et al. 2006). However, the majority of the observed BHXB systems only have one or two X-ray observations in quiescence, usually separated by years. Thus, it is difficult to provide definitive statements on the details of how the X-ray spectral softening occurs on a case-by-case basis.

We initially focus on archival *Chandra* observations of three BHXB systems (H 1743–322, MAXI J1659–152, and XTE J1752–223). The observations were taken as part of joint *Chandra* and Very Large Array (VLA) target of opportunity (TOO) programs (PI: P. G. Jonker). These Jonker et al. TOO programs were approved over several *Chandra* cycles to monitor individual BHXB systems at the tail end of an outburst (H 1743–322 was observed during *Chandra* cycle-9, XTE J1752–223 during cycle-11, and MAXI J1659–152 during cycle-12). The observations were triggered once a radio counterpart was identified and the X-ray flux dropped below a certain threshold (usually 10^{-11} – 10^{-10} erg s $^{-1}$ cm $^{-2}$ from 0.5 to 10 keV, which typically corresponds to $l_x < 10^{-4}$), with a preference toward observing systems with low line of sight hydrogen column densities. Usually four to eight (nearly) simultaneous *Chandra* X-ray and VLA radio observations were taken within 30 days of triggering. The *Chandra* observations were designed to obtain enough counts to allow for imaging spectroscopy, making an archival study based on these TOO programs ideal for studying the X-ray spectral evolution of transient BHXBs as they fade into quiescence, as both a function of time and luminosity.

The data for H 1743–322, MAXI J1659–152, and XTE J1752–223 were originally published in Jonker et al. (2010), Jonker et al. (2012), and Ratti et al. (2012), respectively. These publications focus on the evolution of each source’s radio/X-ray luminosity during the fade into quiescence, while here we instead focus on their X-ray spectral evolution. After tracking the spectral evolution for the above individual systems, we then compare their spectral properties to other BHXB systems with available X-ray spectra at $l_x < 10^{-4}$ in the literature. Simultaneously examining all available X-ray spectra provides new insight into how (and at what X-ray luminosity) black holes transition into quiescence, and whether or not quiescence is simply an extension of the low–hard state. Our sample and data reduction are described in Section 2; the best-fit X-ray spectral properties are presented in Section 3, and our results are discussed and summarized in Section 4 and Section 5, respectively. All reported X-ray luminosities are unabsorbed (i.e., corrected for the effects of extinction) and calculated from 0.5 to 10 keV by integrating over each observation’s best-fit power-law spectrum, and all quoted measurement uncertainties are at the 68% level (i.e., $\Delta\chi^2 = 1.0$ for one parameter of interest).

2. CHANDRA X-RAY OBSERVATIONS

2.1. Chandra Data Reductions and Spectral Fitting

There are a total of 18 unique *Chandra* observations covering H 1743–322 (8 observations taken in 2008 March), MAXI J1659–152 (6 observations taken from 2011 April to October), and XTE J1752–223 (4 observations taken from 2010 July to August). Each source’s properties are given in Table 1, and the *Chandra* observations (including the ObsIDs) are summarized in Table 2. We note that Jonker et al. carried out similar joint *Chandra*/VLA TOO programs for two other sources, XTE J1908+094 (cycle-4) and V4641 Sgr (cycle-5). However, only three X-ray observations were taken for XTE J1908+094. Only one of these three observations has $l_x < 10^{-4}$, and that observation has too few counts to fit an X-ray spectrum (see Jonker et al. 2004). We thus do not consider XTE J1908+094 here. V4641 Sgr typically shows an unusually hard X-ray spectrum while in outburst (e.g., Maitra & Bailyn 2006), and this hard spectrum apparently persists even in our quiescent *Chandra* observations. Given its odd behavior, we do not consider V4641 Sgr here and we defer a discussion on V4641 Sgr in quiescence to a future paper (E. Gallo et al., in preparation).

We re-analyze all 18 observations to ensure that our data reductions are as uniform as possible from source to source, and that the latest calibration is applied to each observation. The target is always placed on the back-illuminated S3 chip of the Advanced CCD Imaging Spectrometer (ACIS) detector (Garmire et al. 2003). To help avoid photon pileup, the ACIS-S3 CCD is windowed to read out only the 1/8 chip subarray, except for four observations of H 1743–322 (ObsIDs 8990, 9837, 9838, and 9839) that use the 1/2 chip subarray. We reprocessed and analyzed all data with the CIAO4.4 software (Fruscione et al. 2006) developed by the Chandra X-Ray Center, employing the latest calibration files from data base version 4.5.3. We used the *chandra_repro* script to reprocess the raw data, and we created custom bad pixel maps for each observation. Six of our longest exposures (ObsIDs 8990, 9837, 9838, 9839, 11056, and 12443) were taken in VFAINT data mode. For these observations, pulse height information in a 5×5 pixel region (instead of a 3×3 pixel region) is telemetered down, allowing for a more rigorous cleaning of background events (e.g., caused by cosmic rays, etc.). Unless otherwise stated, we only consider events with photon energies between 0.5 and 7 keV to minimize the ACIS high-energy particle background. All data are used, since we do not see any evidence for background flares. All 18 *Chandra* observations contain a detection of the target source, typically with tens to hundreds of counts (see Table 2).

We extract source counts and spectra within circular apertures centered on accurately known sky positions for each source (see Table 1). We generally use 2 arcsec radius extraction regions. However, in order to enclose a sufficiently high number of total source counts, we adopt 3 arcsec radius apertures for two observations of H 1743–322 (ObsIDs 8987 and 8988) and for one observation of XTE J1752–223 (ObsID 12310). We similarly adopt a 5 arcsec radius aperture for one observation of MAXI J1659–152 (ObsID 12441). Finally, our longest exposures for XTE J1752–223 (ObsIDs 11055 and 11056) reveal faint sources very close to the source position.⁷ We thus use 1.5 arcsec radius apertures for these two observations. To

⁷ Some of these faint sources appear to be extended X-ray jet emission (Ratti et al. 2012).

Table 1
Source Parameters

Source Name	R.A. (J2000)	Decl. (J2000)	$N_H \times 10^{22}$ (cm^{-2})	Mass ^a (M_\odot)	Distance (kpc)	P_{orb} (hr)	Inclination (deg)
Sources from Jonker et al. <i>Chandra</i> TOO programs							
H 1743–322	17 ^h 46 ^m 15 ^s .61	−32°14′00″.6(1)	2.3(2,3)	...	8.5 ± 0.8(4)	≥10(3)	75 ± 3(4)
MAXI J1659–152	16 ^h 59 ^m 01 ^s .68	−15°15′28″.7(5)	0.23(6,7)	...	6 ± 2(7)	2.4(6,8)	60–75(6)
XTE J1752–223	17 ^h 52 ^m 15 ^s .09	−22°20′32″.4(9)	0.5(10,11)	9.6 ± 0.9(12)	3.5–8(11)	≤6.8(11)	<49(9,13)
Other systems with <i>Chandra</i> X-ray spectra							
A 0620–00	06 ^h 22 ^m 44 ^s .54	−00°20′44″.4(14)	0.194(15)	11.0 ± 1.9(16)	1.16 ± 0.11(16)	7.75(17)	40.75 ± 3(16)
GRO J1655–40	16 ^h 54 ^m 00 ^s .20	−39°50′43″.6(18)	0.859(15)	6.3 ± 0.6(19)	3.2 ± 0.2(20,21)	62.92(20,21)	70.2 ± 1.9(19)
GX 339–4	17 ^h 02 ^m 49 ^s .50	−48°47′23″.0(22)	0.6(23)	5.8 ± 0.5(24)	8 ± 4(21,25)	42.1(24)	<60(26)
V404 Cyg ^b	20 ^h 24 ^m 03 ^s .82	33°52′01″.9(27,28)	0.81(29,30)	12 ± 2(31)	2.39 ± 0.14(28)	155.28(32)	56 ± 4(31)
XTE J1118+480 ^c	11 ^h 18 ^m 10 ^s .85	48°02′12″.9(33)	0.012(34)	6.9–8.2(35)	1.72 ± 0.10(36)	4.08(37)	68–79(35)
XTE J1550–564	15 ^h 50 ^m 58 ^s .78	−56°28′35″.0(38)	0.9(39,40)	9.10 ± 0.61(41)	4.38 ^{+0.58} _{−0.41} (41)	37.03(41)	74.7 ± 3.8(47)
XTE J1650–500	16 ^h 50 ^m 00 ^s .98	−49°57′43″.6(42)	0.67(42)	<7.5(43)	2.6 ± 0.7(44)	7.7(43)	>50 ± 3(43)

Notes.^a We assume $M = 10 M_\odot$ for H 1743–322 and MAXI J1659–152.^b V404 Cyg has a proper motion of $\mu_\alpha \cos \delta = -5.04 \pm 0.02$ milliarcsec yr^{−1} and $\mu_\delta = -7.64 \pm 0.02$ milliarcsec yr^{−1}. The coordinates given in Columns 2 and 3 are referenced to MJD 54322 (Miller-Jones et al. 2009).^c XTE J1118+480 has a proper motion of $\mu_\alpha = -16.8 \pm 1.6$ milliarcsec yr^{−1} and $\mu_\delta = -7.4 \pm 1.6$ milliarcsec yr^{−1} (Mirabel et al. 2001). The coordinates given in columns 2 and 3 are referenced to MJD 51635 (Garcia et al. 2000).

References. (1) Steeghs et al. 2003; (2) Miller et al. 2006b; (3) Jonker et al. 2010; (4) Steiner et al. 2012; (5) Paragi et al. 2010; (6) Kennea et al. 2011; (7) Jonker et al. 2012; (8) Kuulkers et al. 2010; (9) Miller-Jones et al. 2011b; (10) Curran et al. 2011; (11) Ratti et al. 2012; (12) Shaposhnikov et al. 2010; (13) Reis et al. 2011; (14) Gallo et al. 2006; (15) Kong et al. 2002; (16) Gelino et al. 2001; (17) McClintock & Remillard 1986; (18) Hjellming et al. 1994; (19) Greene et al. 2001; (20) Jonker & Nelemans 2004; (21) Dunn et al. 2010; (22) Reynolds & Miller 2013; (23) Corbel et al. 2013; (24) Hynes et al. 2003; (25) Zdziarski et al. 2004; (26) Cowley et al. 2002; (27) Miller-Jones et al. 2008; (28) Miller-Jones et al. 2009; (29) Bradley et al. 2007; (30) Corbel et al. 2008; (31) Shahbaz et al. 1994; (32) Casares et al. 1992; (33) Garcia et al. 2000; (34) McClintock et al. 2003; (35) Khargharia et al. 2013; (36) Gelino et al. 2006; (37) Cook et al. 2000; (38) Jain et al. 1999; (39) Tomsick et al. 2001; (40) Corbel et al. 2006; (41) Orosz et al. 2011; (42) Tomsick et al. 2004; (43) Orosz et al. 2004; (44) Homan et al. 2006.

Table 2
Log of *Chandra* X-Ray Observations Tracking Individual Outburst Decays

ObsID	Obs. Date	MJD (day; UTC)	Time on Source (ks)	Net Count Rate 0.5–7 keV (counts s ^{−1})	Net Source Counts	Background Counts
H 1743–322						
8987	2008 Mar 2	54527.13111	6.5	$(9.92 \pm 0.41) \times 10^{-2}$	643.0	1.0
8988	2008 Mar 8	54533.69200	13.7	$(1.80 \pm 0.12) \times 10^{-2}$	247.8	1.2
8989	2008 Mar 16	54541.23027	20.5	$(3.56 \pm 0.47) \times 10^{-3}$	73.2	0.8
9833	2008 Mar 17	54542.08033	11.0	$(2.04 \pm 0.53) \times 10^{-3}$	22.5	0.5
9838	2008 Mar 21	54546.42945	23.8	$(1.74 \pm 0.32) \times 10^{-3}$	41.4	0.6
8990	2008 Mar 22	54547.32918	21.2	$(1.29 \pm 0.30) \times 10^{-3}$	27.4	0.6
9839	2008 Mar 23	54548.30002	28.7	$(1.19 \pm 0.24) \times 10^{-3}$	34.1	0.9
9837	2008 Mar 24	54549.22579	20.6	$(1.58 \pm 0.33) \times 10^{-3}$	32.5	0.5
MAXI J1659–152						
12438	2011 Apr 14	55665.96202	6.4	$(3.73 \pm 0.26) \times 10^{-2}$	236.8	0.2
12439	2011 Apr 23	55674.74944	9.1	$(8.67 \pm 1.09) \times 10^{-3}$	78.7	0.3
12440	2011 May 3	55684.29844	13.6	$(5.61 \pm 2.91) \times 10^{-4}$	7.6	0.4
12441	2011 May 12	55693.21054	18.1	$(6.74 \pm 0.06) \times 10^{-1}$	12226.4	6.6
12442	2011 Aug 15	55788.83283	30.8	$(3.31 \pm 1.44) \times 10^{-4}$	10.2	0.8
12443	2011 Oct 12	55846.53179	90.7	$(4.34 \pm 0.82) \times 10^{-4}$	39.3	1.7
XTE J1752–223						
11053	2010 Jul 12	55389.63924	6.4	$(3.43 \pm 0.91) \times 10^{-3}$	21.8	0.2
12310	2010 Jul 20	55397.07034	13.6	$(3.86 \pm 0.18) \times 10^{-2}$	525.5	1.5
11055	2010 Jul 26	55403.24698	31.4	$(6.16 \pm 1.77) \times 10^{-4}$	19.4	0.6
11056	2010 Aug 2	55410.27430	88.9	$(8.04 \pm 1.08) \times 10^{-4}$	71.5	1.5

Note. Data were originally published in Jonker et al. (2010), Jonker et al. (2012), and Ratti et al. (2012) for H 1743–322, MAXI J1659–152, and XTE J1752–223, respectively.

Table 3
Best-fit Spectral Parameters for *Chandra* Observations Tracking Outburst Decays

ObsID	MJD (day; UTC)	Γ^a	Unabs. 0.5–10 keV Flux ^{a,b} (erg cm ⁻² s ⁻¹)	l_x^c	Goodness ^d
H 1743–322					
8987	54527.13111	1.75 ± 0.15	$(4.0 \pm 0.7) \times 10^{-12}$	2×10^{-5}	0.31
8988	54533.69200	1.81 ± 0.23	$(7.4 \pm 1.9) \times 10^{-13}$	4×10^{-6}	0.43
8989	54541.23027	2.02 ± 0.53	$(1.8 \pm 1.0) \times 10^{-13}$	9×10^{-7}	0.55
9833 ^e	54542.08033	1.53 ± 0.5	8×10^{-14}	5×10^{-7}	...
9838	54546.42945	$1.54^{+0.41}_{-0.75}$	$(8.7^{+3.7}_{-5.5}) \times 10^{-14}$	5×10^{-7}	0.50
8990	54547.32918	$2.14^{+0.36}_{-0.90}$	$(6.0 \pm 5.3) \times 10^{-14}$	3×10^{-7}	0.57
9839	54548.30002	1.30 ± 0.78	$(4.6^{+4.3}_{-2.2}) \times 10^{-14}$	2×10^{-7}	0.34
9837	54549.22579	$3.15^{+0.40}_{-0.59}$	$(1.6^{+0.5}_{-0.9}) \times 10^{-13}$	8×10^{-7}	0.27
MAXI J1659–152					
12438	55665.96202	2.11 ± 0.23	$(4.6 \pm 0.8) \times 10^{-13}$	2×10^{-6}	0.50
12439	55674.74944	1.79 ± 0.39	$(1.2 \pm 0.3) \times 10^{-13}$	4×10^{-7}	0.89
12440 ^e	55684.29844	2.26 ± 0.5	6×10^{-15}	2×10^{-8}	...
12441 ^f	55693.21054	$1.55^{+0.04}_{-0.02}$	$(1.3 \pm 0.02) \times 10^{-11}$	4×10^{-5}	0.60
12441 ^g	55693.21054	1.74 ± 0.33	$(1.2^{+0.1}_{-0.2}) \times 10^{-11}$	4×10^{-5}	0.89
12442 ^e	55788.83283	2.25 ± 0.5	4×10^{-15}	1×10^{-8}	...
12443	55846.53179	3.25 ± 0.73	$(5.8^{+1.6}_{-1.2}) \times 10^{-15}$	2×10^{-8}	0.65
XTE J1752–223					
11053	55389.63924	2.17 ± 0.95	$(5.2^{+2.9}_{-1.9}) \times 10^{-14}$	1×10^{-7}	0.12
12310	55397.07034	1.75 ± 0.14	$(6.8 \pm 0.8) \times 10^{-13}$	2×10^{-6}	0.95
11055	55403.24698	$1.64^{+0.53}_{-0.86}$	$(9.7 \pm 6.3) \times 10^{-15}$	2×10^{-8}	0.36
11056	55410.27430	2.20 ± 0.47	$(1.4 \pm 0.5) \times 10^{-14}$	4×10^{-8}	0.13

Notes.

^a Uncertainties are at the 68% level ($\Delta C = 1.0$ for one parameter of interest, where C is the Cash statistic).

^b Unabsorbed flux calculated by integrating over the best-fit model from 0.5 to 10 keV, excluding the effects of extinction.

^c Normalized Eddington ratio $l_x = L_{0.5-10\text{ keV}}/L_{\text{Edd}}$.

^d A goodness value around 0.50 indicates a good fit to the data. We fit an absorbed power law to 10^4 simulated spectra based on the best-fit parameters to each data set. The goodness is the fraction of fits with a lower Cash statistic than our best fit to the real data set.

^e Effective photon indices and fluxes are estimated from X-ray band ratios using PIMMS.

^f Fit with Davis (2001) pileup model has best-fit pileup parameter $\alpha = 0.12 \pm 0.11$ (estimated pileup fraction $f_{\text{pile}} = 0.021$).

^g Fit to readout streak with 201 source photons (see Section 2.1.1).

extract sky counts, we use a circular annulus with a 10 arcsec inner radius and a 20 arcsec outer radius whenever possible. However, some observations have faint sources within these radii. So, for all four observations of XTE J1752–223 (ObsIDs 11053, 11055, 11056, and 12310) we use a 12 arcsec inner radius and an 18 arcsec outer radius; for our two longest exposures of MAXI J1659–152 (ObsIDs 12442 and 12443) we use a 6 arcsec inner radius and a 15 arcsec outer radius. Since one observation of MAXI J1659–152 (ObsID 12441) shows readout streaks related to its high count rate (see Section 2.1.1), we extract sky counts for this observation using a 15 arcsec radius circular aperture centered on a source-free region of the CCD near the target source. This off-source aperture avoids source photons from the streak potentially contaminating our sky background.

X-ray spectra are extracted using *specextract* in CIAO. We create background and source response matrix files and auxiliary response files for each observation, applying an energy-dependent point-source aperture correction to the latter to account for the fraction of enclosed energy within our adopted source apertures. Spectra are then fit using ISIS version 1.6.2-10 (Houck & Denicola 2000). We include background counts in our fits using Cash statistics (Cash 1979),⁸ adopting an absorbed

power-law model for all sources (i.e., *phabs*powerlaw*).⁹ We only allow the power-law normalization and photon index (Γ) to vary as free parameters, fixing the hydrogen column density N_{H} to the same values adopted in our previous work on these sources, as listed in Table 1. An absorbed power-law model provides adequate fits, but we note that there are likely other models that could fit equally well. Our primary goal is to compare the spectral shape of several sources at different l_x . Thus, especially given the relatively low number of source counts in most of our observations, an absorbed power law serves as the simplest way to parameterize the X-ray spectral shape, and to then uniformly compare all of our data. Our best-fit spectral parameters are summarized in Table 3, and we note that our best-fit parameters are consistent with the previously published values based on these data.

There are three observations with too few source counts to obtain adequate spectral fits, including one observation for H 1743–322 (ObsID 9833), and two observations for MAXI J1659–152 (ObsIDs 12440 and 12442). We instead estimate effective photon indices for these three observations using

⁸ The Cash statistic converges toward χ^2 when the number of source counts is large.

⁹ For the photoelectric absorption model, we use cross sections from Balucinska-Church & McCammon (1992) with updated He cross sections from Yan et al. (1998), and we use abundances from Anders & Grevesse (1989).

their observed source count rates in soft (0.5–2.0 keV) and hard (2.0–7.0 keV) X-ray bands. Aperture corrections are applied to each band’s count rates to account for the enclosed energy within each circular extraction region (~ 2 arcsec radius apertures enclose an average of $\sim 95\%$ and 88% within the soft and hard bands, respectively). We then use the *Chandra* Portable, Interactive Multi-Mission Simulator (PIMMS; Mukai 1993)¹⁰ to infer effective photon indices, applying the appropriate effective area curves for the *Chandra* cycle when each observation was taken. We also calculate effective photon indices for the 14 observations that have good spectral fits and that do not display signs of photon pileup. By comparing these 14 effective photon indices to their corresponding best-fit (spectroscopic) photon indices, we estimate that our effective photon indices are accurate to approximately ± 0.5 (the maximum difference between the two types of photon index measures).

2.1.1. Photon Pileup

One observation of MAXI J1659–152 (ObsID 12441) has a sufficiently high count rate to suffer from the effects of photon pileup. Here, two or more photons could arrive within a CCD detector region during a single frame time integration (0.4 s for this observation) and subsequently be registered as a single event. We fit this data set in ISIS using the pileup model of Davis (2001). When fitting with the pileup model, we consider all events with energies larger than 0.5 keV.¹¹ We find that the pileup is rather mild, with a pileup fraction $f_{\text{pile}} = 0.021$. This observation also shows a readout streak, which is caused by photons that are collected during the 41 ms it takes to transfer the image into the readout buffer. This streak is not affected by pileup, and it contains sufficient counts that we can extract a source spectrum from the streak photons. Thus, we also extract a streak spectrum, using two $\sim 3 \times 25$ arcsec² boxes located ~ 5 arcsec northeast and southwest of the source position, and we extract sky counts from surrounding regions of size $\sim 60 \times 25$ arcsec² centered on each source extraction box (and excluding streak photons). There are a total of 201 streak source photons.

The effective exposure time for the readout streak data is much lower than the total exposure time, since for each frame time integration of 0.4 s each streak pixel is only exposed for 40 μ s (the time to transfer and read one pixel). Our streak extraction region contains approximately 100 streak pixels, yielding an effective exposure time of 0.004 s per frame. With a total time on source of 18.1 ks, we have a combined $18100/0.4 = 45,250$ frames. The effective streak exposure time is thus approximately $0.004 \times 45,250 = 181$ s. Finally, we create a response matrix file and an auxiliary response file at the location of MAXI J1659–152, using *mkacisrmf* and *mkarf*, respectively (and we adjust the auxiliary response file for the 181 s effective exposure time). Our best spectral fit is consistent with the on-source extraction fit with the pileup model within 1σ , and we include both fits in Table 3. Throughout this paper, we adopt the spectral parameters extracted from the readout streak in order to minimize the number of free parameters to our fit. Our results are similar, however, if we instead use the pileup model best-fit parameters.

2.2. Chandra Spectroscopy of Other Weakly Accreting BHXB Systems

We wish to compare our observations that track three individual BHXBs as they fade into quiescence with as many other systems as possible. Unfortunately, no other system has sufficient X-ray temporal coverage to track their spectral evolution on a case-by-case basis. However, comparison to the ensemble of all other BHXBs observed at $l_x \lesssim 10^{-4}$ will allow additional insight into the average properties of quiescent BHXBs. Only *Chandra* and *XMM-Newton* provide enough sensitivity to obtain X-ray spectra at these very low X-ray luminosities with reasonable exposure times. Searching the *Chandra* and *XMM-Newton* archives, there are only around a dozen BHXBs with adequate observations. The vast majority of observations are with *Chandra* (using ACIS-S imaging spectroscopy), and every source with an *XMM-Newton* spectrum at $l_x \lesssim 10^{-4}$ also has *Chandra* coverage at a similar X-ray luminosity. Thus, in order to keep comparisons between systems as uniform as possible (and to minimize the potential for source confusion due to *XMM-Newton*’s coarser spatial resolution), we decide to directly compare only to other *Chandra*/ACIS-S observations. We re-analyze all archival *Chandra* observations and perform our own spectral fits in order to include the latest calibrations, and also to help alleviate potential systematics that could be introduced by simply combining a heterogeneous set of data reductions directly from the literature.

We require archival *Chandra* observations to contain at least 20 source counts. This constraint adds another 19 *Chandra* observations divided over 7 additional systems (2 observations of A0620–00, 2 observations of GRO J1655–40, 2 observations of GX 339–4, 2 observations of V404 Cyg, 1 observation of XTE J1118+480, 7 observations of XTE J1550–564,¹² and 3 observations of XTE J1650–500). We include basic properties for each source in Table 1, and a log of these 19 *Chandra* X-ray observations can be found in Table 4. We note that the observations were originally taken for primary science purposes different than ours, and we list the publication that first presented each *Chandra* observation in Table 4. Combined with our other 3 BHXB systems in Tables 2 and 3, we have a total of 37 *Chandra* observations covering 10 systems. We note that we do not consider any system that has X-ray observations in quiescence but with too few counts to fit an X-ray spectrum (e.g., many of the systems in Figure 4 of Reynolds & Miller 2011). Nor do we include any X-ray observations of systems at $l_x > 10^{-4}$, since that luminosity regime has already been well explored in the literature (e.g., Wu & Gu 2008).

2.2.1. X-Ray Data Reduction of Other Chandra Observations

We follow identical data reduction and spectral fitting procedures as described in Section 2.1. These archival *Chandra* observations generally have a similar setup as described earlier. However, most observations read out the entire CCD instead of a subarray except for the following: for GX 339–4, ObsID 12410 uses the 1/8 chip subarray; for V404 Cyg, ObsID 97 uses the 1/4 chip subarray and ObsID 3808 uses the 1/8 chip subarray; and for XTE J1550–564, ObsID 3448 uses the 1/4 chip subarray. XTE J1650–500 is fairly bright in all three observations. As described in Tomsick et al. (2004), to reduce

¹⁰ <http://cxc.harvard.edu/toolkit/pimms.jsp>

¹¹ Filtering the data from 0.5 to 7 keV as in the previous section may provide less reliable fits with the pileup model (see http://cxc.harvard.edu/ciao/why/filter_energy.html).

¹² Although there are a total of seven observations for XTE J1550–564, these observations are separated by months to years with similar observed X-ray fluxes. Thus, they do not provide the same opportunity to track X-ray spectral evolution as for H 1743–322, MAXI J1659–152, and XTE J1752–223.

Table 4
Log of Other *Chandra* X-Ray Observations

ObsID	Obs. Date	MJD (day; UTC)	Time on Source (ks)	Net Count Rate 0.5–7 keV (counts s ⁻¹)	Net Source Counts	Background Counts	Ref. ^a
A0620–00							
95	2000 Feb 29	51603.14750	42.1	$(3.20 \pm 0.30) \times 10^{-3}$	134.7	2.3	1,2
5479	2005 Aug 20	53602.35887	39.6	$(8.04 \pm 0.48) \times 10^{-3}$	318.4	1.6	3
GRO J1655–40							
99	2000 Jul 1	51726.79797	42.6	$(1.51 \pm 0.21) \times 10^{-3}$	64.1	0.9	1
10907	2009 Jun 8	54990.10230	18.2	$(9.09 \pm 0.76) \times 10^{-3}$	165.5	0.5	4
GX 339–4							
4445	2003 Sep 29	52911.48765	28.3	$(3.80 \pm 0.12) \times 10^{-2}$	1076.5	1.5	5
12410	2011 May 15	55696.67966	27.2	$(2.63 \pm 0.10) \times 10^{-2}$	715.8	2.2	6
V404 Cyg							
97	2000 Apr 26	51660.68457	10.3	$(1.64 \pm 0.04) \times 10^{-1}$	1689.8	1.2	1,7
3808	2003 Jul 28	52848.86452	55.6	$(3.48 \pm 0.08) \times 10^{-2}$	1933.9	4.1	7
XTE J1118+480							
3422	2002 Jan 12	52286.14907	45.8	$(1.54 \pm 0.21) \times 10^{-3}$	70.7	1.3	2
XTE J1550–564							
1845	2000 Aug 21	51777.36325	5.1	$(1.29 \pm 0.18) \times 10^{-2}$	65.8	0.2	8,1,9
1846	2000 Sep 11	51798.20398	4.6	$(2.41 \pm 0.25) \times 10^{-2}$	109.9	0.1	8,1,9
3448	2002 Mar 11	52344.62513	26.1	$(4.60 \pm 0.14) \times 10^{-2}$	1200.2	4.8	9
3672	2002 Jun 19	52444.37961	18.0	$(3.14 \pm 0.48) \times 10^{-3}$	56.6	0.4	9
3807	2002 Sep 24	52541.83357	24.4	$(8.74 \pm 0.64) \times 10^{-3}$	213.6	0.4	9
4368	2003 Jan 28	52667.18878	23.7	$(1.03 \pm 0.07) \times 10^{-2}$	244.5	0.5	9
5190	2003 Oct 23	52935.30373	47.8	$(3.03 \pm 0.27) \times 10^{-3}$	144.9	1.1	9
XTE J1650–500							
3400	2002 Jan 23	52297.99426	10.0	$(2.76 \pm 0.05) \times 10^{-1}$	2764.5	23.5	10
3401	2002 Feb 4	52309.60891	9.5	$(2.73 \pm 0.05) \times 10^{-1}$	2595.0	19.0	10
2731	2002 Mar 2	52335.09478	18.3	$(5.02 \pm 0.05) \times 10^{-1}$	9177.9	10.1	10

Notes.

^a References where data were previously published: (1) Kong et al. 2002; (2) McClintock et al. 2003; (3) Gallo et al. 2006; (4) Calvelo et al. 2010; (5) Gallo et al. 2003a; (6) Corbel et al. 2013; (7) Corbel et al. 2008; (8) Tomsick et al. 2001; (9) Corbel et al. 2006; (10) Tomsick et al. 2004.

pileup the first two observations (ObsIDs 3400 and 3401) were taken with the High Energy Transmission Grating Spectrometer (HETGS) in place. The third observation (ObsID 2731) did not use the HETGS (since there were fewer counts per second), but to mitigate pileup the 1/8 chip subarray was used and XTE J1650–500 was also placed 2.7 arcmin off-axis to blur the point-spread function. For the HETGS observations, we reduce the zero-order images. The effects of pileup are still present in all three observations of XTE J1650–500, but none show a readout streak with sufficient counts to extract a spectrum.

Most of the 19 observations are taken in FAINT data mode, except ObsIDs 3422 (XTE J1118+480) and 10097 (GRO J1655–40) that are taken in VFAINT data mode. We again extract source counts using 2 arcsec radius circular apertures (centered on the known source positions listed in Table 1), and we extract sky counts using circular annuli with inner and outer radii of 10 and 20 arcsec, respectively. However, for A0620–00 (ObsIDs 95 and 5479), GX 339–4 (ObsIDs 4445 and 12410), and V404 Cyg (ObsIDs 97 and 3808) we instead extract source counts with a 3 arcsec radius circular aperture, since there are a relatively larger number of source counts in these observations. For A0620–00, we extract sky counts using a circular annulus with a 15 arcsec inner radius and a 25 arcsec outer radius in order to avoid nearby sources. XTE J1550–564 has a relatively large number of source counts in ObsID 3448 (~1200 photons); for

this observation we thus extract source counts using a 5 arcsec radius circular aperture. XTE J1550–564 is also in a particularly crowded field (e.g., it is the first BHXB with the detection of X-ray jets, which were originally discovered from these *Chandra* observations; Corbel et al. 2002; Tomsick et al. 2003). We thus extract sky counts in all seven observations of XTE J1550–564 using a 20 arcsec radius circular aperture centered on a nearby source-free region of the CCD in each image. Finally, for XTE J1650–500 we use a 5 arcsec radius circular aperture to extract source counts from ObsID 2731 and 10 arcsec radius circular apertures for ObsIDs 3400 and 3401 in order to enclose a large number of source counts; we use circular annuli with a 20 arcsec inner radius and a 30 arcsec outer radius for all three observations of XTE J1650–500.

After extracting spectra for each source, we fit absorbed power laws to each spectrum, and we use the Davis (2001) pileup model for all three XTE J1650–500 observations. These three observations have pileup fractions of $f_{\text{pile}} = 0.098$ (ObsID 2731), 0.34 (ObsID 3400), and 0.32 (ObsID 3401), and our best-fit spectral parameters are similar (within the errors) to those obtained by Tomsick et al. (2004). We fix the hydrogen column density in each fit to the values listed in Table 1. The best-fit spectral parameters are listed in Table 5, which are consistent with previously published values at the 1 σ level. We note that our best-fit photon index for the 2000 observation of V404 Cyg

Table 5
Best-fit Spectral Parameters for Other *Chandra* X-Ray Observations

ObsID	MJD (day; UTC)	Γ^a	Unabs. 0.5–10 keV Flux ^{a,b} (erg cm ⁻² s ⁻¹)	I_x^c	Goodness ^d
A 0620–00					
95	51603.14750	2.00 ± 0.25	$(3.0 \pm 0.5) \times 10^{-14}$	4×10^{-9}	0.81
5479	53602.35887	2.24 ± 0.16	$(8.9 \pm 0.9) \times 10^{-14}$	1×10^{-8}	0.32
GRO J1655–40					
99	51726.79797	$1.78^{+0.45}_{-0.26}$	$(3.9^{+0.8}_{-1.6}) \times 10^{-14}$	6×10^{-8}	0.72
10907	54990.10230	$1.93^{+0.13}_{-0.24}$	$(2.1 \pm 0.5) \times 10^{-13}$	3×10^{-7}	0.58
GX 339–4					
4445	52911.48765	2.02 ± 0.09	$(6.3^{+0.4}_{-0.3}) \times 10^{-13}$	7×10^{-6}	0.42
12410	55696.67966	1.98 ± 0.11	$(4.7 \pm 0.4) \times 10^{-13}$	5×10^{-6}	0.80
V404 Cyg					
97	51660.68457	$2.00^{+0.04}_{-0.07}$	$(3.2^{+0.1}_{-0.2}) \times 10^{-12}$	2×10^{-6}	0.15
3808	52848.86452	$2.13^{+0.04}_{-0.07}$	$(7.0 \pm 0.4) \times 10^{-13}$	5×10^{-7}	0.54
XTE J1118+480					
3422	52286.14907	$2.09^{+0.34}_{-0.22}$	$(9.7^{+0.8}_{-1.7}) \times 10^{-15}$	4×10^{-9}	0.56
XTE J1550–564					
1845	51777.36325	$2.38^{+0.25}_{-0.52}$	$(2.8^{+0.6}_{-0.9}) \times 10^{-13}$	8×10^{-7}	0.52
1846	51798.20398	2.21 ± 0.39	$(5.7^{+0.9}_{-1.4}) \times 10^{-13}$	2×10^{-6}	0.53
3448	52344.62513	$2.27^{+0.05}_{-0.08}$	$(9.3^{+0.8}_{-0.3}) \times 10^{-13}$	3×10^{-6}	0.88
3672	52444.37961	$2.57^{+0.25}_{-0.57}$	$(7.8^{+1.8}_{-2.8}) \times 10^{-14}$	2×10^{-7}	0.55
3807	52541.83357	$2.08^{+0.08}_{-0.15}$	$(1.9 \pm 0.4) \times 10^{-13}$	6×10^{-7}	0.53
4368	52667.18878	$2.14^{+0.15}_{-0.10}$	$(2.4^{+0.2}_{-0.3}) \times 10^{-13}$	7×10^{-7}	0.64
5190	52935.30373	2.23 ± 0.28	$(6.8 \pm 1.4) \times 10^{-14}$	2×10^{-7}	0.71
XTE J1650–500					
3400 ^e	52297.99426	1.67 ± 0.10	$(4.4^{+2.2}_{-0.9}) \times 10^{-11}$	4×10^{-5}	0.86
3401 ^f	52309.60891	1.64 ± 0.10	$(4.3^{+4.9}_{-0.9}) \times 10^{-11}$	4×10^{-5}	0.82
2731 ^g	52335.09478	2.09 ± 0.07	$(9.9 \pm 0.3) \times 10^{-12}$	9×10^{-6}	0.40

Notes.

^a Uncertainties are at the 68% level ($\Delta C = 1.0$ for one parameter of interest, where C is the Cash statistic).

^b Unabsorbed flux calculated by integrating over the best-fit model from 0.5 to 10 keV, excluding the effects of extinction.

^c Normalized Eddington ratio $I_x = L_{0.5-10\text{keV}}/L_{\text{Edd}}$.

^d A goodness value around 0.50 indicates a good fit to the data. We fit an absorbed power law to 10^4 simulated spectra based on the best-fit parameters to each data set. The goodness is the fraction of fits with a lower Cash statistic than our best fit to the real data set.

^e Fit with Davis (2001) pileup model has best-fit pileup parameter $\alpha = 0.77 \pm 0.23$ (estimated pileup fraction $f_{\text{pile}} = 0.34$).

^f Fit with Davis (2001) pileup model has best-fit pileup parameter $\alpha = 0.73 \pm 0.27$ (estimated pileup fraction $f_{\text{pile}} = 0.32$).

^g Fit with Davis (2001) pileup model has best-fit pileup parameter $\alpha = 0.95^{+0.05}_{-0.08}$ (estimated pileup fraction $f_{\text{pile}} = 0.098$).

(ObsID 97) is significantly softer than the photon index first published by Kong et al. (2002). That observation was likely affected by mild pileup in the original analysis, as pointed out by Corbel et al. (2008). With improved reprocessing algorithms in CIAO, the pileup is much less severe in our data reductions. Our best-fit spectral parameters for this observation are consistent with the spectral parameters presented in Corbel et al. (2008), and we additionally find that including the Davis (2001) pileup model does not substantially improve our fit.

2.3. Effect of Fixing Column Density in the Spectral Fits

Since we do not have enough counts to directly fit for N_H in all 37 *Chandra* observations, we fix N_H to values obtained from the literature (as referenced in Table 1). These column densities were generally estimated from higher signal-to-noise X-ray spectra at higher I_x , with N_H left as a free parameter. Advantages of adopting these N_H values include easier comparison to the literature (since these column densities are often used in

other studies), and usually smaller statistical errors on N_H than could be obtained from our data. However, there are also disadvantages. For one, we must assume that N_H remains relatively constant during the outburst decay. Most importantly though, fixing N_H to predetermined values could systematically bias our best-fit photon indices, since using a larger or smaller N_H would cause us to overestimate or underestimate Γ , respectively. To illustrate the potential magnitude of this effect, we took each system's *Chandra* observation with the highest number of counts (or the second highest number of counts for MAXI J1659–152 to avoid pileup), and we refit that spectrum allowing N_H to vary as a free parameter. In Figure 1, we show confidence contour maps of Γ versus N_H for each of these fits. For comparison, we also show the best-fit values of Γ obtained from fixing N_H (filled circles; i.e., these circles show the Γ values listed in Tables 3 and 5). We omit XTE J1118+480 from Figure 1 because it has an extremely small column density, and any systematic effect would be negligible.

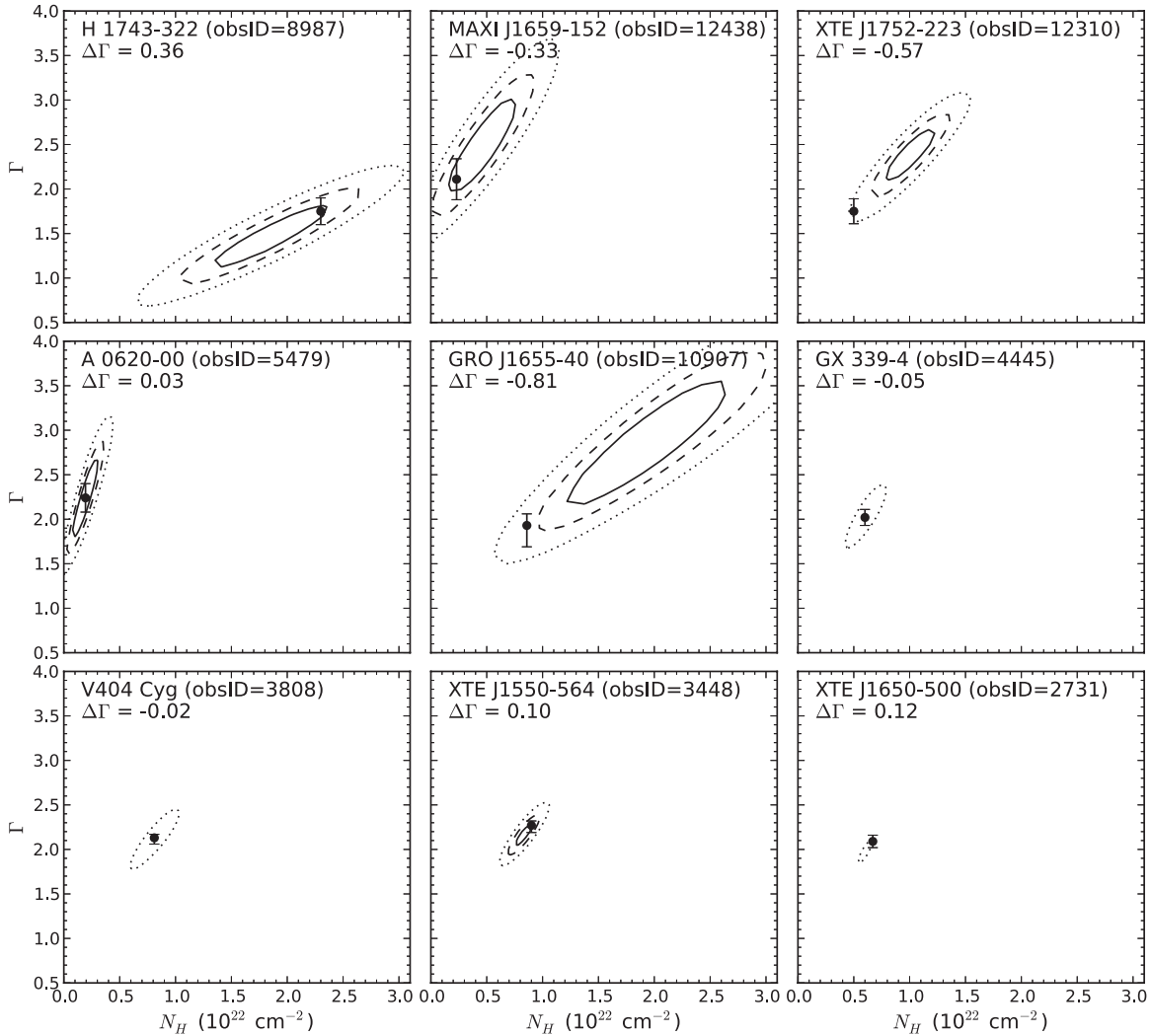


Figure 1. Confidence contour maps of photon index (Γ) vs. hydrogen column density (N_H), allowing N_H to vary as a free parameter for each system’s *Chandra* observation with the largest number of counts (the second highest for MAXI J1659–152 to avoid pileup). We omit XTE J1118+480 because of its very small column density. The solid, dashed, and dotted lines show changes in the Cash statistic (ΔC) of 2.30, 4.61, and 9.21, respectively (i.e., the 68%, 90%, and 99% confidence intervals for two parameters of interest). For clarity, we only draw the 99% contour for GX 339–4, V404 Cyg, and XTE J1650–500. The filled circles show the best-fit Γ values when fixing N_H to the values adopted in the text (see Table 1). The difference between the best-fit Γ when fixing N_H and when allowing N_H to vary is reported as $\Delta\Gamma = \Gamma(N_{H,\text{fixed}}) - \Gamma(N_{H,\text{free}})$ in the top left corner of each panel in order to (roughly) quantify the systematic uncertainty that could be introduced by fixing N_H to the values in Table 1.

The difference between the best-fit photon indices keeping N_H fixed versus allowing N_H to vary is given in the top left corner of each panel as $\Delta\Gamma = \Gamma(N_{H,\text{fixed}}) - \Gamma(N_{H,\text{free}})$. $\Delta\Gamma$ provides an estimate of the magnitude of any potential systematic bias on Γ that could be present for each system (although we note that $\Delta\Gamma$ is approximate, its value is specific to each observation and would not be identical for every observation of the corresponding system). For about half of the systems, $\Delta\Gamma$ is close to zero and we do not expect a significant systematic bias. Not surprisingly, the systems with the largest $\Delta\Gamma$ (H 1743–322, MAXI J1659–152, XTE J1752–223, and GRO J1655–40) also tend to have the fewest number of counts (and therefore the largest uncertainty in N_H). Thus, we opt to always adopt N_H values from the literature for the reasons described earlier, but keeping in mind that this could force a systematic bias at a level shown in Figure 1.

3. RESULTS

In Figure 2, we show the temporal evolution of Γ and l_x for the decays of H 1743–322, MAXI J1659–152, and

XTE J1752–223. The *Chandra* observations cover Eddington ratios between $l_x \sim 10^{-9}$ – 10^{-4} . Each source’s X-ray luminosity eventually levels off, indicating that each system has very likely reached quiescence during the observations. Also, MAXI J1659–152 underwent a small flare after it reached quiescence. There is strikingly little evolution of Γ during each decay, even when MAXI J1659–152 is flaring. According to Wu & Gu (2008), BHXBs attain their hardest X-ray spectra ($\Gamma \sim 1.5$) around $l_x \sim 10^{-2}$. As BHXBs fade, their spectra soften with decreasing luminosity. We find that this Γ – l_x anti-correlation does not extend to all $l_x < 10^{-4}$, but it eventually saturates to a value near $\Gamma \sim 2$ (Figure 3). Such a saturation in quiescence was also suggested by Sobolewska et al. (2011).

In Figure 4(a), we add the other 19 *Chandra* observations (see Section 2.2) to the Γ – l_x plane. For clarity, we also show the same plot binned by l_x in panel 4(b). Γ does not appear to continue to soften at low l_x in the full sample either. The 37 observations in Figure 4 have a Spearman rank correlation coefficient of $\rho = -0.323$ with $p = 0.051$, indicating that there is no statistically significant anti-correlation between Γ

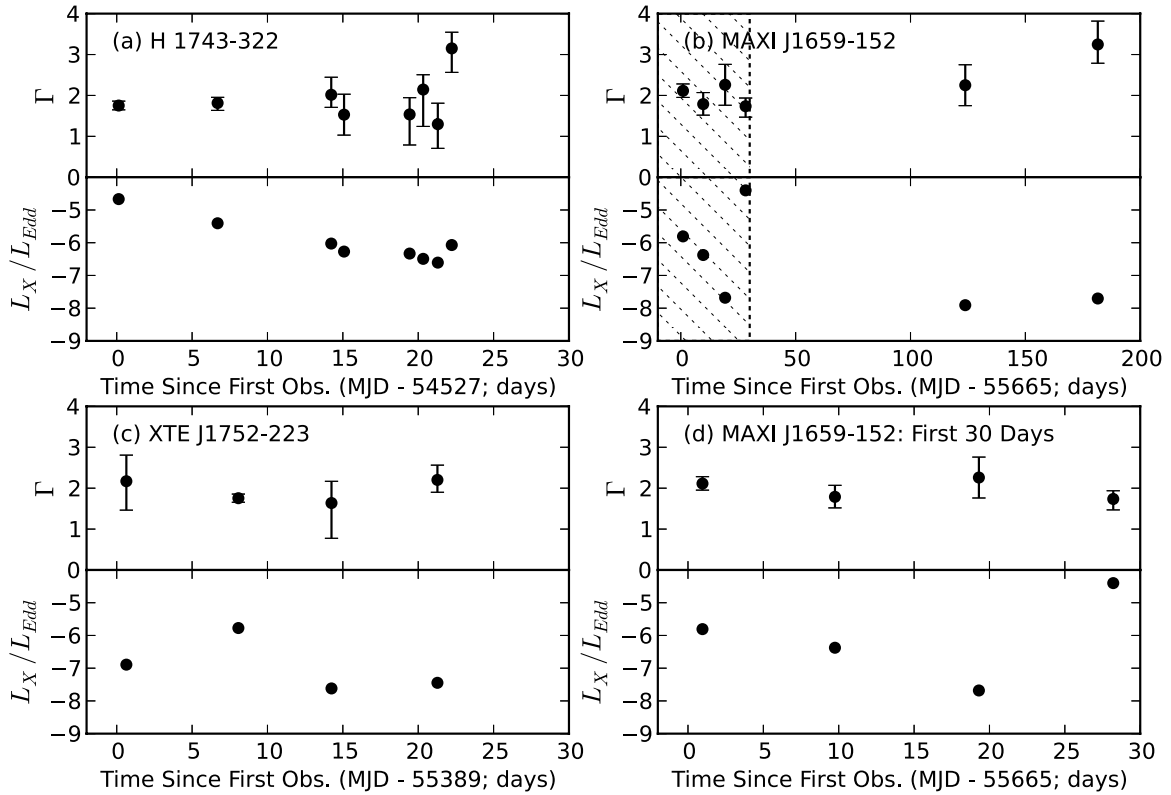


Figure 2. Each panel shows photon index vs. time (top) and normalized Eddington ratio vs. time (bottom) for our three sources with multiple *Chandra* observations at the tail end of an outburst. Each panel’s x-axis begins when the first *Chandra* observation was taken. Panel (b) shows all data for MAXI J1659–152, while panel (d) shows the same data zoomed in for only the first 30 days of observations (covering the hatched region in panel (b)). MAXI J1659–152 underwent a small flare during its decay into quiescence. Otherwise, each source reaches quiescence fairly quickly, and there is no obvious spectral evolution.

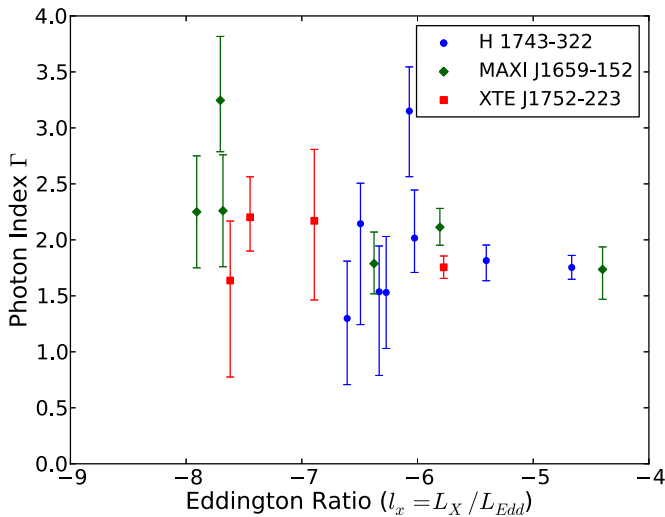


Figure 3. Photon index vs. Eddington ratio for three systems with decays covered by *Chandra*.

(A color version of this figure is available in the online journal.)

and l_x at $l_x < 10^{-4}$. We cannot definitively identify the precise luminosity where Γ begins to saturate. However, judging from Figure 4, $l_x \sim 10^{-5}$ could be a reasonable threshold. We only have four data points at $l_x > 10^{-5}$, but all four have similar $\Gamma < 2$ and an average $\langle \Gamma \rangle = 1.70 \pm 0.03$ (although we note one of these data points is from MAXI J1659–152 during its mini-flare). This $\langle \Gamma \rangle$ is harder than the average photon index for our remaining 33 observations at $l_x < 10^{-5}$, which have $\langle \Gamma \rangle = 2.08 \pm 0.07$. Plus, the possibility of an anti-correlation

between Γ and l_x is even less statistically significant for these 33 observations ($\rho = -0.162$ and $p = 0.368$). Thus, the Γ – l_x anti-correlation observed for low–hard state BHXBs does not appear to continue into quiescence, and Γ seems to plateau by the time l_x reaches $\sim 10^{-5} L_{\text{Edd}}$.

For the 33 observations at $l_x \lesssim 10^{-5}$, we measure a relatively large scatter about Γ of $\sigma_{\text{int}} = \pm 0.39$ (with σ_{int}^2 defined as the variance about the mean $\langle \Gamma \rangle$ divided by $N - 1$). This scatter may partly be caused by a low level of variability in quiescence, but it is more likely that the scatter is primarily due to measurement uncertainty in Γ (resulting from the relatively low number of counts in each spectrum). To illustrate that the scatter could primarily be statistical noise, we randomly draw 33 photon indices from a normal distribution with $\langle \Gamma \rangle = 2.08$ and a standard deviation of ± 0.35 (the latter is a typical measurement uncertainty in Γ from our spectral fits). We then measure the scatter of these 33 randomly drawn photon indices about their mean. We repeat 10^5 times, and 17% of our simulated Γ distributions have $|\sigma_{\text{int}}| > 0.39$. We also perform a more detailed test by simulating 10^3 X-ray spectra with ~ 70 counts (typical of our observations) using an absorbed power-law model with $N_{\text{H}} = 5 \times 10^{21} \text{ cm}^{-2}$ and $\Gamma = 2.08$. We then fit the simulated spectra, keeping N_{H} fixed but allowing Γ to vary. The distribution for the 10^4 best-fit Γ has $\sigma_{\text{int}} = \pm 0.35$, which is comparable to the observed σ_{int} for the 33 observations. We also repeat the simulations for 10^3 spectra with ~ 30 counts and 10^4 spectra with ~ 200 counts, which show $\sigma_{\text{int}} = \pm 0.55$ and ± 0.23 , respectively. Since the observed scatter is likely dominated by the lowest-count spectra, measurement uncertainty can easily explain the observed scatter. Thus, to the accuracy of our data, all of the BHXB systems have a similar photon index at $l_x \lesssim 10^{-5}$.

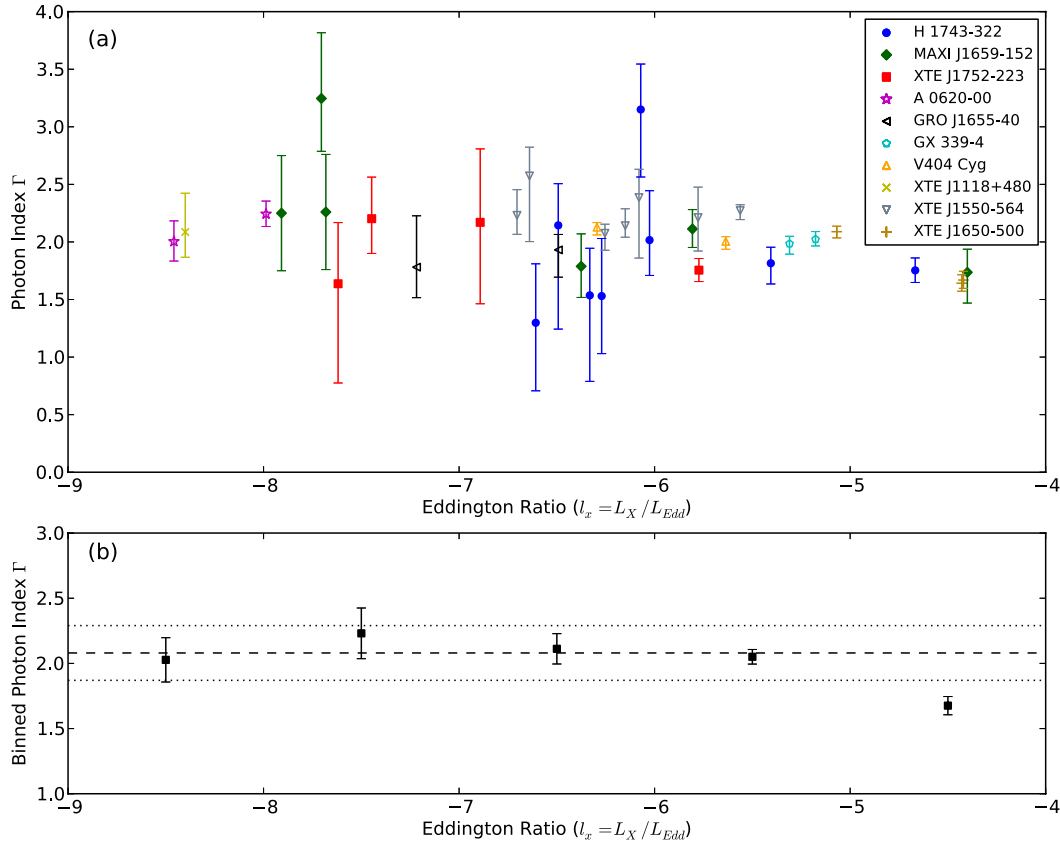


Figure 4. (a) Same as Figure 3 but for all 10 BHXB systems. (b) Same data binned by Eddington ratio for clarity. There is no obvious spectral evolution at $l_x \lesssim 10^{-5}$ on average. The dashed line in panel (b) marks the average $\langle \Gamma \rangle = 2.08$ for all observations at $l_x < 10^{-5}$, and the dotted lines show $\pm 3\sigma$ deviations. In the highest luminosity bin, Γ is harder by 5.9σ , indicating that the X-ray spectral softening from the low-hard state heading into quiescence takes place over a relatively small range in l_x .

(A color version of this figure is available in the online journal.)

3.1. Eddington Ratios and Photon Indices at the Lowest Luminosities

The lowest observed X-ray luminosity for each source represents the source's properties deep in quiescence, and the corresponding Eddington ratio and photon index are interesting properties. Four systems (GRO J1655-40, XTE J1118+480, XTE J1650-500, and V404 Cyg) have a single observation that is easily identified as having the lowest observed X-ray luminosity. Some of our systems, however, have multiple *Chandra* observations at similarly low X-ray luminosities. Thus, to calculate the smallest Eddington ratios and corresponding photon indices, we averaged all data with $L_X < 10^{33.5} \text{ erg s}^{-1}$ for H 1743-322 (six observations), with $L_X < 10^{32} \text{ erg s}^{-1}$ for MAXI J1659-152 (three observations), with $L_X < 10^{32} \text{ erg s}^{-1}$ for XTE J1752-223 (two observations), and with $L_X < 10^{32.5} \text{ erg s}^{-1}$ for XTE J1550-564 (two observations). For A0620-00 and GX 339-4, we average both observations for each system. The resulting photon indices and Eddington ratios for all 10 systems are shown in Figure 5. We again see no trend between Γ and Eddington ratio, supporting that (on average) BHXB X-ray spectral properties deep in quiescence do not strongly depend on X-ray luminosity.

4. DISCUSSION

4.1. X-Ray Emission Mechanisms in Quiescence

The fact that we see X-ray emission from quiescent BHXBs indicates that there is still some amount of matter falling onto the

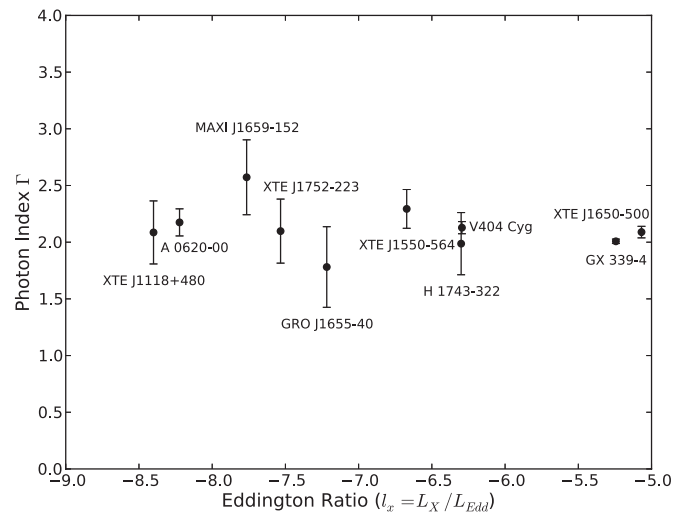


Figure 5. Photon index vs. Eddington ratio at the lowest observed X-ray luminosity for each system (see Section 3.1).

black hole even at low l_x (the X-ray emission is unlikely from the corona of the secondary star; see, e.g., the discussion in Narayan & McClintock 2008). The plateau of Γ at low l_x may represent a spectral signature for when a BHXB enters the quiescent state. Our data suggest that there is either a gradual change in accretion disk structure/geometry between $l_x \sim 10^{-2}$ and at least 10^{-5} , or that the relevant high-energy radiative processes saturate at some

critical luminosity. There is currently no standardly adopted luminosity threshold in the literature for when a BHXB enters quiescence (see Remillard & McClintock 2006), and we propose $l_x < 10^{-5}$ as an observationally motivated upper luminosity limit for quiescence.

In the canonical picture for low-hard state BHXBs, some form of a hot, geometrically thick, radiatively inefficient accretion flow (RIAF) is typically invoked for the inner regions of the accretion disk (e.g., Esin et al. 1997). RIAFs (and geometrically thick disks in general) are prone to developing outflows (e.g., Rees et al. 1982; Narayan & Yi 1994, 1995; Blandford & Begelman 1999; Livio et al. 1999; Igumenshchev et al. 2000; Meier et al. 2001; Hawley & Balbus 2002; Narayan 2005), which is consistent with radio observations that imply that low-hard state black holes ubiquitously launch compact jets (e.g., Corbel et al. 2000, 2004; Stirling et al. 2001; Miller-Jones et al. 2008; Fender et al. 2009). In an RIAF, the amount of X-ray radiation scales nonlinearly with accretion rate ($L_x \sim \dot{m}^q$, typically with $q \sim 2$ in the simplest cases). Thus, only a small amount of the accretion energy is liberated as radiation, thereby resulting in an underluminous accretion disk compared to a standard cold disk. The observed (hard) X-rays are then generated from a combination of inverse Comptonization of lower-energy photons off a hot population of electrons (e.g., Malzac et al. 2001; Gilfanov 2010), and also a likely contribution from jet-related processes (e.g., Falcke & Biermann 1995; Markoff et al. 2001, 2003, 2005; Maitra et al. 2009).

There are many variants of RIAFs in the literature,¹³ and the advection-dominated accretion flow (ADAF; e.g., Narayan & Yi 1994; Abramowicz et al. 1995) has been particularly successful for modeling the spectra of quiescent BHXBs (e.g., Narayan et al. 1996, 1997; Hameury et al. 1997). In an ADAF, the Coulomb coupling between electrons and ions is weak, resulting in a two-temperature plasma, with hot populations of thermal electrons and ions at characteristic temperatures T_e and T_i , respectively (with $T_e < T_i$). ADAF models predict an X-ray spectral softening as BHXBs fade into quiescence (e.g., Esin et al. 1997; Qiao & Liu 2013). For example, Esin et al. (1997) show that as l_x decreases, the optical depth of the hot electrons will decrease and therefore so does the Compton-y parameter. Thus, as a BHXB fades from the low-hard state into quiescence, there is less inverse Compton scattering and fewer hard X-rays are emitted (i.e., the X-ray spectra become softer). The observed inflection point in the BHXB Γ - l_x plane at $l_x \sim 10^{-2}$ is likely due to a switch in the source of Comptonized seed photons (e.g., Kalemci et al. 2005; Sobolewska et al. 2011; Gardner & Done 2012). Thermal seed photons from a cold accretion disk dominate at $l_x \gtrsim 10^{-2}$, while a different source of seed photons dominate at lower l_x (e.g., cyclo-synchrotron from the hot accretion flow or synchrotron self-Compton are two possibilities).

Esin et al. (1997) predict that the softening of the X-ray spectrum (from 1 to 10 keV) peaks at $\Gamma \sim 2.2$. Then in quiescence, inverse Compton scattering becomes so weak that bremsstrahlung radiation will start to dominate the hard X-rays, which will slightly re-harden the X-ray spectrum to $\Gamma \sim 1.7$ (which is harder than our X-ray observations on average, but not inconsistent given our individual error bars). Yuan & Cui (2005) point out that at low accretion rates ($l_x \lesssim 10^{-5}$ – 10^{-6}) the jet should start to dominate in the X-ray, instead of bremsstrahlung.

They consider an ADAF coupled to a compact steady-state jet, and they include radiative losses from synchrotron cooling in their jet. We expect such synchrotron cooled radiation to follow a power law with $\Gamma \sim 2$, also consistent with our observations. Since the jet spectrum is a power law, we would naturally expect Γ to plateau in quiescence. We note that Gardner & Done (2012) also include a jet in their RIAF model for BHXBs, but they do not find that the jet ever dominates quiescent X-ray spectra. However, Gardner & Done (2012) do not include synchrotron cooling losses in their model.

The shape of the spectrum is a major difference between jet-dominated and RIAF-dominated emission models. Jets should produce power-law X-ray spectra in quiescence, while ADAF X-ray spectra (and spectra from most types of RIAFs in general) should be curved since their hard X-rays are inverse Compton scattered off of a thermal distribution of electrons.¹⁴ An interesting prediction of RIAF models is that, since electrons have higher T_e and lower optical depth in quiescence, one expects to see multiple Compton peaks (opposed to the low-hard state where multiple Compton peaks merge together into one broad hump; McClintock et al. 2003). Thus, the amount of curvature expected in quiescent X-ray spectra depends on which scattering order falls into the X-ray band. Unfortunately, there is not any existing X-ray spectrum that can sufficiently constrain the X-ray spectral shape well enough to differentiate between jet and RIAF X-ray origins.

Finally, we note that there is evidence, at least for more luminous low-hard state BHXBs ($l_x \gtrsim 10^{-3}$), that a standard cold accretion disk could always extend close to the innermost stable circular orbit (ISCO; e.g., Miller et al. 2006a, 2012; Malzac 2007; Wilkinson & Uttley 2009; Reynolds & Miller 2010; Reis et al. 2010; Uttley et al. 2011). However, in quiescence, the accretion flow is so underluminous that it seems unlikely that a cold accretion disk could be present close to the ISCO. We do not see an obvious soft X-ray component that would require the addition of a cold disk to our spectral models (although it is not clear if such a component could be easily seen in our low-count spectra). Regardless, in quiescence, the standard picture invoking an RIAF in the inner regions (and a standard disk in the outer regions) with the addition of a possible jet component seems plausible. However, we stress that there are other possibilities (also, see, e.g., Merloni & Fabian 2002; Xie & Yuan 2012).

4.2. On the Transition from the Low-Hard State into Quiescence

Many low-hard state BHXBs show a relatively tight nonlinear correlation between radio and X-ray luminosity (Corbel et al. 2003; Gallo et al. 2003b; although see Gallo et al. 2012), which may imply a coupling between the accretion flow and the radio jet. The observed radio emission is optically thick (i.e., self-absorbed) synchrotron radiation from a compact steady jet. In order to explain the observed slope of the luminosity correlation, the X-ray radiation must be inefficient with $L_x \sim \dot{m}^2$ (Gallo et al. 2003b; Markoff et al. 2003, 2005). Such inefficient X-ray emission is consistent with either an RIAF (Merloni et al. 2003) or with optically thin jet synchrotron emission (Markoff et al. 2003; Falcke et al. 2004; Plotkin et al. 2012b). The radio/X-ray luminosity correlation has also been extended to include the optical and infrared (OIR) wavebands (Homan

¹³ For example, the advection-dominated inflow-outflow solution (Blandford & Begelman 1999) and convection-dominated accretion flows (Narayan et al. 2000; Quataert & Gruzinov 2000).

¹⁴ However, a curved X-ray spectrum is not expected from RIAF models with non-thermal electron distributions.

et al. 2005; Russell et al. 2006; Coriat et al. 2009). OIR/X-ray correlations also imply a coupling between the disk and jet (with the OIR dominated by non-thermal jet radiation and/or reprocessed disk emission).

The compact steady jet has three main components. At the lowest frequencies is the optically thick part showing a flat or inverted spectrum, as is typically observed in the radio. At higher frequencies the jet becomes optically thin (usually around the infrared for a $\sim 10 M_\odot$ black hole), typically showing Γ between 1.5 and 1.7. Finally, at the highest frequencies the jet becomes synchrotron cooled (i.e., radiation losses become so large that the emitting particles lose kinetic energy), where we expect Γ to steepen (i.e., increase) by ~ 0.5 . Considering this expected shape for the jet's broadband spectrum and the $\langle \Gamma \rangle = 2.08$ observed from our sample, if the jet dominates in the X-ray waveband in quiescence, then we expect that jet emission should already be synchrotron cooled. In this case, the observed X-ray luminosity will scale *linearly* with \dot{m} (e.g., Heinz 2004; Yuan & Cui 2005), instead of approximately *quadratically* as with either RIAF or optically thin jet synchrotron. Then, the slope of the radio/X-ray luminosity correlation should be different in quiescence, as suggested by Yuan & Cui (2005) who predict that the correlation steepens to $L_R \sim L_X^{1.23}$ below $l_x \lesssim 10^{-5}$ – 10^{-6} (the exact slope and transition luminosity depend on specific model parameters). One would similarly expect the OIR/X-ray correlation to steepen as well.

Exactly how the transition to synchrotron cooled dominated X-rays occurs depends on the frequency of the jet cooling break ν_{cool} (i.e., the frequency where the jet transitions from being optically thin to synchrotron cooled). If ν_{cool} is always below the X-ray band, then RIAF emission could dominate in the low-hard state (with $L_X \sim \dot{m}^2$) and the synchrotron cooled part of the jet would dominate in quiescence (with $L_X \sim \dot{m}$). However, it is unclear if ν_{cool} always falls at such low frequencies, and therefore if such a transition from RIAF to synchrotron cooled X-ray emission actually occurs in nature. For example, at least some low-hard state BHXBs can have optically thin synchrotron emission extending into the X-ray waveband (e.g., Markoff et al. 2001; Russell et al. 2010). Also, in several hard-state systems, a high-energy break that could be associated with synchrotron cooling has been observed at a few tens of keV (i.e., above the *Chandra* X-ray band, although that break could instead be associated with cooling from Comptonization; see Pe'er & Markoff 2012).

Given the above uncertainties on the location of ν_{cool} , another plausible scenario to explain the observed spectral softening is that ν_{cool} is above X-ray energies in most low-hard state BHXBs. Then, as BHXBs fade into quiescence, ν_{cool} shifts through the X-ray band. In this case, X-rays could always be jet dominated, but jet X-rays would be optically thin synchrotron in the low-hard state and synchrotron cooled in quiescence. Russell et al. (2013) isolate the frequency where jets transition from optically thick to optically thin for 12 BHXBs at various l_x (this optically thin transition happens at lower frequencies than the cooling break, namely, 10^{12} – 10^{14} Hz). The optically thin jet break is related to the location along the jet where particles are accelerated into a non-thermal distribution (see, e.g., Polko et al. 2013). From their sample, Russell et al. (2013) speculate that the higher-energy cooling break ν_{cool} could shift from hard X-ray energies at $l_x \sim 10^{-3}$ to the ultraviolet at $l_x \sim 10^{-5}$. However, more observations are needed to determine how ν_{cool} evolves as BHXBs fade into quiescence, especially since factors other than \dot{m} are almost certainly important for determining the

evolution of ν_{cool} and jet properties in general. For example, if the magnetic field B at the location along the jet where synchrotron radiative losses become important depends *only* on \dot{m} , then one would expect the exact opposite evolution where ν_{cool} should instead increase with decreasing \dot{m} .¹⁵ Also, general relativistic magnetohydrodynamic simulations show that beyond \dot{m} , the geometry of the magnetic field threading the disk close to the black hole can influence whether a strong collimated jet is even launched in the first place (McKinney & Blandford 2009; Dibi et al. 2012). There is also the possibility of inverse Compton scattering off of jet particles contributing to the observed X-ray emission (either from synchrotron or external seed photons). Thus, the expected evolution of ν_{cool} as BHXBs fade into quiescence is unclear, and more detailed studies are needed.

Further complicating matters is that the radio/X-ray luminosity correlation for low-hard state BHXBs is not as universal as once thought. Recently, there have been discoveries of several outliers to the “standard” correlation, such that at a given X-ray luminosity these outliers are fainter in the radio than expected (e.g., Corbel et al. 2004; Brocksopp et al. 2005; Cadolle Bel et al. 2007; Jonker et al. 2010; Soleri et al. 2010; Ratti et al. 2012). There is now statistical evidence for two tracks within the radio/X-ray luminosity correlation, with the “standard” track following $L_r \sim L_X^{0.63}$ and the “radio-faint” track following a steeper slope $L_r \sim L_X^{0.98}$ (Gallo et al. 2012). It is interesting that the only two systems with firm simultaneous radio and X-ray detections in quiescence—A0620–00 at $l_x \sim 10^{-8.5}$ (Gallo et al. 2006) and V404 Cyg at $l_x \sim 10^{-6.6}$ (Gallo et al. 2005; Miller-Jones et al. 2008)—fall along the “standard track” extrapolated to low l_x . All other efforts to detect radio emission in quiescence have only yielded upper limits so far, and we have not yet seen any conclusive evidence for radio-faint BHXBs at $l_x \lesssim 10^{-5}$ (see Miller-Jones et al. 2011a and references therein. Also see Figure 9 of Corbel et al. 2013 for a recent radio/X-ray correlation including radio-faint systems). Some low-hard state BHXB systems (including H 1743–322, MAXI J1659–152, and XTE J1752–223 in our sample) have even been observed to switch from the “radio-faint” track to the “standard track” by the time they reach $l_x \sim 10^{-5}$ (e.g., Jonker et al. 2010, 2012; Coriat et al. 2011; Ratti et al. 2012). While perhaps coincidental, it is potentially interesting that the “radio-faint” track seems to end around the same l_x where we find Γ saturates in our BHXB sample. We speculate that this similarity in l_x could imply that the same type of high-energy emission processes tend to dominate in most quiescent systems, while there is potentially more variety in the low-hard state (although further work is needed; see, e.g., Calvelo et al. 2010).

4.3. Orbital Parameters

There is a well-known relationship between the lowest observed X-ray luminosity deep in quiescence and orbital period, where BHXB systems with the faintest X-ray luminosities have the shortest periods (e.g., Lasota & Hameury 1998; Menou et al. 1999; Garcia et al. 2001).¹⁶ The X-ray luminosity–period relationship indicates that for systems with shorter periods, the

¹⁵ The typical Lorentz factor of a synchrotron cooled electron is $\gamma_{\text{cool}} \sim (B^2 t_{\text{cool}})^{-1}$, where t_{cool} is the dynamical cooling timescale (e.g., Rybicki & Lightman 1979; Heinz 2004). Thus, $\nu_{\text{cool}} \sim B \gamma_{\text{cool}}^2 \sim \dot{m}^{-3/2}$, if $B^2 \sim \dot{m}$ (as expected for a mechanically cooled flow; Heinz & Sunyaev 2003).

¹⁶ A trend between X-ray luminosity and orbital period is also observed for neutron star X-ray binaries although neutron star systems are more luminous than BHXBs at comparable orbital periods.

secondary star transfers less mass per unit time onto the accretion disk (assuming that a similar fraction of transferred mass eventually accretes onto the black hole in all systems). The mass transfer rate is expected to depend on orbital period, since systems with similar orbits are likely to have similar types of secondary stars (with similar mass-loss rates). Also, different mechanisms may drive the mass transfer at different orbital periods. For example, see Section 3 of Menou et al. 1999 (and references therein) for a discussion on angular momentum losses from gravitational radiation (and perhaps magnetic braking) at short orbital periods compared to mass loss driven by the secondary’s nuclear evolution at longer periods.

Our 10 systems are consistent with the X-ray luminosity–period relationship (although see Jonker et al. 2012 regarding MAXI J1659–152 perhaps being brighter than expected). One might thus expect that the orbit could also affect the shape of quiescent BHXB spectra, as proposed by Corbel et al. (2006) who found that three long-period systems (GRO J1655–40, V404 Cyg, and V4641 Sgr) show harder X-ray spectra deep in quiescence compared to shorter-period systems. However, we do not see any trend between our 10 systems’ Γ at their faintest L_X and their orbital parameters (specifically period and inclination; see Figure 6). The lack of a dependence of Γ on orbital parameters is consistent with the conclusion of Corbel et al. (2008), who re-examined the quiescent properties of V404 Cyg, which is the source that (statistically) dominated the earlier Corbel et al. (2006) study. Although we find that GRO J1655–40 may be slightly harder than other quiescent BHXB systems, it is not harder at a statistically significant level.¹⁷ The final source with a hard quiescent X-ray spectrum in Corbel et al. (2006), V4641 Sgr, really does seem to stay hard in quiescence. However, a power law appears to be a poor fit to *Chandra* observations of this source at low L_X , and its hard spectrum is unlikely driven by orbital period. We will discuss this interesting source in more detail in a future paper (E. Gallo et al., in preparation).

In summary, the orbital period and rate of mass transfer can affect the total amount of emitted X-rays. However, by the time matter reaches the inner regions of the accretion flow, it is apparently the properties/geometry of the accretion disk (and potential connections to any outflow) that most strongly control how the X-rays are produced. In other words, the accretion disk feeding mechanism may determine the X-ray “normalization,” but it does not strongly affect the emission mechanism deep in quiescence. A similar argument would suggest that black hole spin is also unlikely very important for controlling X-ray spectral properties in quiescence.

4.4. Comparisons to Supermassive Black Holes

Changes in \dot{m} not only affect the accretion states of BHXBs, but also may be partly responsible for different subclasses of AGNs. For example, the “standard track” of the BHXB radio/X-ray luminosity correlation can be extended to include supermassive black holes by incorporating an additional mass

normalization term (i.e., the fundamental plane of black hole activity; Merloni et al. 2003; Falcke et al. 2004). Supermassive analogs to low-hard state black holes include low-luminosity AGNs (LLAGNs) and low-luminosity radio galaxies (i.e., FR Is and BL Lac objects; e.g., Falcke et al. 2004; Plotkin et al. 2012b). These supermassive analogs do not usually show strong “big blue bumps,” indicating significantly weaker disk emission than expected from a standard cold accretion disk (Ho 2008). Like low-hard state BHXBs, these AGNs also tend to show compact radio emission from a jet (e.g., Nagar et al. 2005; Sikora et al. 2007), and their X-ray emission can usually be modeled with a hot inner accretion flow like an RIAF (sometimes with a potential jet contribution; e.g., Quataert et al. 1999; Nemmen et al. 2006; Ptak et al. 2004; Yu et al. 2011). “Low-hard state” AGNs also tend to show weak broad emission lines and dusty tori, which can also be explained (at least qualitatively) by invoking an RIAF (e.g., Nicastro 2000; Ghisellini & Celotti 2001; Elitzur & Shlosman 2006; Plotkin et al. 2012a).

In addition to the above similarities, LLAGNs also show an anti-correlation between l_x and Γ at low l_x that is similar to the observed anti-correlation for low-hard state BHXBs (Constantin et al. 2009; Gu & Cao 2009; Younes et al. 2011; Gültekin et al. 2012; although also see Winter et al. 2009).¹⁸ We would thus expect supermassive black holes’ hard X-ray photon indices to also plateau when they are in an analogous quiescent state. LLAGNs with $10^{-8} \lesssim l_x \lesssim 10^{-4}$ generally show $1.5 \lesssim \Gamma \lesssim 2.5$ (e.g., Soria et al. 2006; Zhang et al. 2009; Younes et al. 2011), consistent with our expectations. However, a similar type of plateau at very low l_x is yet to be seen, which could be due to a combination of large error bars and not enough source statistics.

5. SUMMARY

We followed the X-ray spectral evolution of three BHXB systems (H 1743–322, MAXI J1659–152, and XTE J1752–223) with *Chandra* during the final parts of their outburst decays. We focus on $l_x \lesssim 10^{-4}$ here because BHXB X-ray spectral properties are relatively unconstrained in this luminosity regime. While these three systems’ X-ray spectra are softer than typical low-hard state BHXBs, there is little to no spectral evolution for these three systems at $l_x \lesssim 10^{-4}$. We compare these systems to all other BHXB systems with available *Chandra* spectral coverage at $l_x \lesssim 10^{-4}$, adding another seven systems to our sample. We find that the anti-correlation between Γ and l_x in the low-hard state at $l_x \lesssim 10^{-2}$ does not extend all the way into quiescence. Rather, by the time a BHXB reaches $l_x \sim 10^{-5}$, its X-ray spectrum saturates to $\langle \Gamma \rangle \sim 2.08 \pm 0.07$ on average (with the observed scatter about $\langle \Gamma \rangle$ likely dominated by measurement error). Our BHXB X-ray spectra do not appear to depend on the binary systems’ orbital parameters. Therefore, it is probably not the feeding mechanism but rather the properties of the accretion flow itself that most strongly determine how X-rays are produced. The similar Γ observed for each quiescent BHXB system, and the lack of any “radio-faint” BHXBs observed at $l_x \lesssim 10^{-5}$ so far, might indicate that there is less variety in X-ray processes in quiescence compared to the low-hard state. However, more studies are needed. Based on the X-ray spectral properties of our low- l_x BHXB sample, $l_x \sim 10^{-5}$ seems to be

¹⁷ Corbel et al. (2006) include a harder $\Gamma = 1.30^{+0.34}_{-0.41}$ data point for GRO J1655–40 in their study, which they took from Hameury et al. (2003). This harder Γ may be due to the choice of column density, as it was obtained by fixing $N_H = 6.7 \times 10^{21} \text{ cm}^{-2}$ when fitting an *XMM-Newton* spectrum. Hameury et al. (2003), however, also obtain a steeper $\Gamma = 1.54^{+1.02}_{-0.72}$ when allowing N_H to vary as a free parameter. In this work, we adopt a slightly larger column density of $N_H = 8.1 \times 10^{21} \text{ cm}^{-2}$ when fitting our *Chandra* spectra, which yields a steeper Γ (and we show in Figure 1 that we might still be systematically underestimating both N_H and Γ , if anything).

¹⁸ AGNs emit a much smaller fraction of their bolometric luminosity in the X-ray waveband compared to BHXBs, which studies focusing on AGNs take into account through bolometric corrections. Here, we continue to use the l_x notation even for AGNs simply for convenience (instead of $L_{\text{bol}}/L_{\text{Edd}}$).

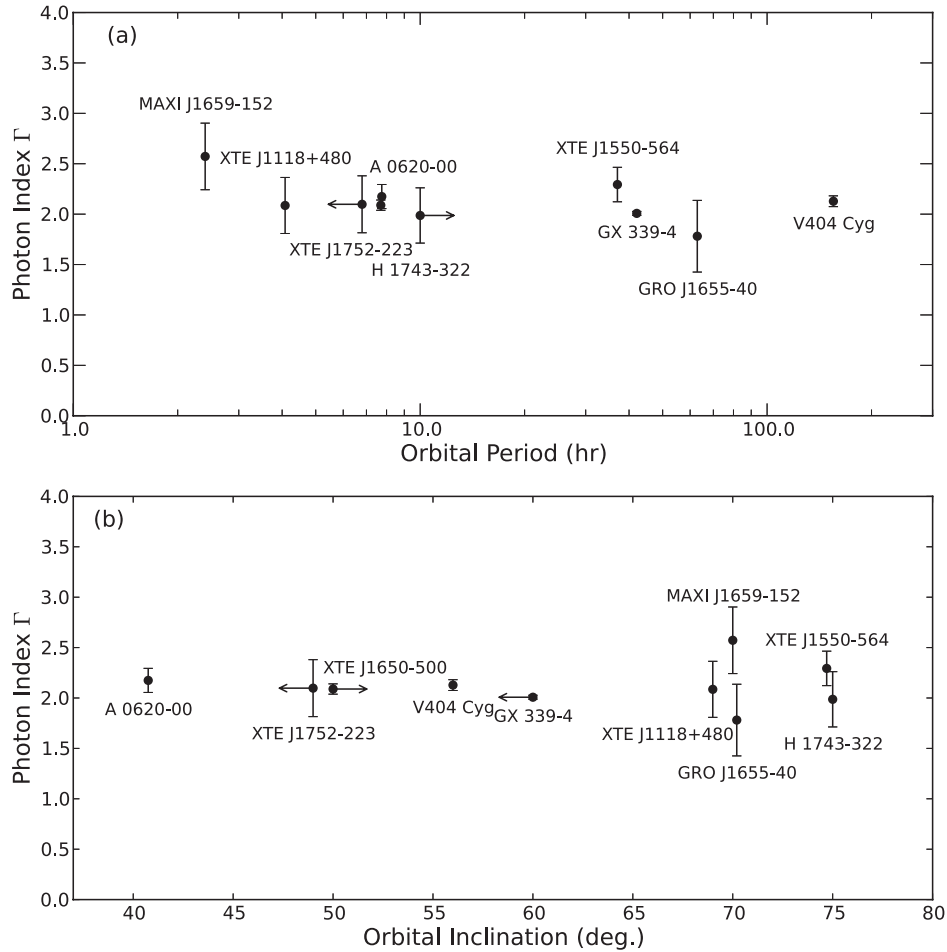


Figure 6. There is no dependence of Γ on the binary system orbital parameters. (a) Γ at the lowest observed X-ray luminosity vs. orbital period. The label for XTE J1650–500 at $P = 7.7$ hr is omitted for clarity. (b) Γ vs. inclination.

an observationally motivated luminosity threshold for when a BHXB enters the quiescent state.

In the future, higher signal-to-noise X-ray spectra than currently available will be critical in order to distinguish between RIAF and jet-dominated X-rays (e.g., most RIAF models predict curved X-ray spectra, while jets predict pure power laws). X-ray polarimetry would also constrain the geometry of the emission regions (Laurent et al. 2011). In order to determine if BHXBs switch from RIAF to jet-dominated X-ray emission in quiescence, more radio constraints are needed to measure the slope of BHXB radio/X-ray correlations in quiescence (e.g., Yuan & Cui 2005), and also to continue to search for “radio-faint” BHXBs at $l_x \lesssim 10^{-5}$ (Miller-Jones et al. 2011a). More observational constraints on the location of the jet synchrotron cooling break (which might be possible with the *Nuclear Spectroscopic Telescope Array*) would also be helpful.

Is quiescence an extension of the low-hard state or rather a distinct spectral state? Although we argue that the plateau in Γ at $l_x \lesssim 10^{-5}$ is an observational signature that a BHXB has entered quiescence, we cannot easily envision a scenario where the observed plateau in Γ indicates a very significant change in the accretion flow. That is, there are subtle differences between the observed emission from quiescent and low-hard state BHXBs, and there is thus some value to thinking of quiescence as its own spectral state. However, quiescence does not appear to represent a distinct spectral state to the same degree as the soft-to-hard or the hard-to-soft transitions at higher l_x . As BHXBs fade, either a jet’s cooling break shifting through the

X-ray band or inverse Compton processes becoming less dominate (owing to lower optical depths) can potentially explain their X-ray emission. Regardless of the right answer, though, the basic accretion disk/outflow structure and geometry is likely the same in quiescence as in the low-hard state.

We thank the anonymous referee for helpful comments that improved this manuscript. We also thank Stéphane Corbel for discussions regarding GX 339–4. Support for this work was provided by the National Aeronautics and Space Administration through Chandra Award Nos. GO1-12049A and GO1-12049A issued by the Chandra X-Ray Observatory Center, which is operated by the Smithsonian Astrophysical Observatory for and on behalf of the National Aeronautics Space Administration under contract NAS8-03060. P.G.J. acknowledges support from the Netherlands Organisation for Scientific Research. This research has made use of data obtained from the Chandra Data Archive and the Chandra Source Catalog, and software provided by the Chandra X-Ray Center (CXC) in the application packages CIAO, ChIPS, and Sherpa.

REFERENCES

- Abramowicz, M. A., Chen, X., Kato, S., Lasota, J.-P., & Regev, O. 1995, *ApJL*, **438**, L37
- Anders, E., & Grevesse, N. 1989, *GeCoA*, **53**, 197
- Balucinska-Church, M., & McCammon, D. 1992, *ApJ*, **400**, 699
- Belloni, T., Homan, J., Casella, P., et al. 2005, *A&A*, **440**, 207
- Blandford, R. D., & Begelman, M. C. 1999, *MNRAS*, **303**, L1

- Bradley, C. K., Hynes, R. I., Kong, A. K. H., et al. 2007, *ApJ*, **667**, 427
- Brocksopp, C., Corbel, S., Fender, R. P., et al. 2005, *MNRAS*, **356**, 125
- Cadolle Bel, M., Ribó, M., Rodriguez, J., et al. 2007, *ApJ*, **659**, 549
- Calvelo, D. E., Fender, R. P., Russell, D. M., et al. 2010, *MNRAS*, **409**, 839
- Casares, J., Charles, P. A., & Naylor, T. 1992, *Natur*, **355**, 614
- Cash, W. 1979, *ApJ*, **228**, 939
- Constantin, A., Green, P., Aldcroft, T., et al. 2009, *ApJ*, **705**, 1336
- Cook, L., Patterson, J., Buczynski, D., & Fried, R. 2000, *IAUC*, **7397**, 2
- Corbel, S., Coriat, M., Brocksopp, C., et al. 2013, *MNRAS*, **428**, 2500
- Corbel, S., Fender, R. P., Tomsick, J. A., Tzioumis, A. K., & Tingay, S. 2004, *ApJ*, **617**, 1272
- Corbel, S., Fender, R. P., Tzioumis, A. K., et al. 2000, *A&A*, **359**, 251
- Corbel, S., Fender, R. P., Tzioumis, A. K., et al. 2002, *Sci*, **298**, 196
- Corbel, S., Koerding, E., & Kaaret, P. 2008, *MNRAS*, **389**, 1697
- Corbel, S., Nowak, M. A., Fender, R. P., Tzioumis, A. K., & Markoff, S. 2003, *A&A*, **400**, 1007
- Corbel, S., Tomsick, J. A., & Kaaret, P. 2006, *ApJ*, **636**, 971
- Coriat, M., Corbel, S., Buxton, M. M., et al. 2009, *MNRAS*, **400**, 123
- Coriat, M., Corbel, S., Prat, L., et al. 2011, *MNRAS*, **414**, 677
- Cowley, A. P., Schmidtke, P. C., Hutchings, J. B., & Crampton, D. 2002, *AJ*, **123**, 1741
- Curran, P. A., Maccarone, T. J., Casella, P., et al. 2011, *MNRAS*, **410**, 541
- Davis, J. E. 2001, *ApJ*, **562**, 575
- Dibi, S., Drappeau, S., Fragile, P. C., Markoff, S., & Dexter, J. 2012, *MNRAS*, **426**, 1928
- Dunn, R. J. H., Fender, R. P., Körding, E. G., Belloni, T., & Cabanac, C. 2010, *MNRAS*, **403**, 61
- Ebisawa, K., Ogawa, M., Aoki, T., et al. 1994, *PASJ*, **46**, 375
- Elitzur, M., & Shlosman, I. 2006, *ApJL*, **648**, L101
- Esin, A. A., McClintock, J. E., & Narayan, R. 1997, *ApJ*, **489**, 865
- Falcke, H., & Biermann, P. L. 1995, *A&A*, **293**, 665
- Falcke, H., Körding, E., & Markoff, S. 2004, *A&A*, **414**, 895
- Fender, R., Belloni, T., & Gallo, E. 2005, *Ap&SS*, **300**, 1
- Fender, R. P., Belloni, T. M., & Gallo, E. 2004, *MNRAS*, **355**, 1105
- Fender, R. P., Homan, J., & Belloni, T. M. 2009, *MNRAS*, **396**, 1370
- Fender, R. P., Maccarone, T. J., & Heywood, I. 2013, *MNRAS*, **430**, 1538
- Fruscione, A., McDowell, J. C., Allen, G. E., et al. 2006, *Proc. SPIE*, **6270**, 60
- Gallo, E., Fender, R., & Corbel, S. 2003a, *ATel*, **196**, 1
- Gallo, E., Fender, R. P., & Hynes, R. I. 2005, *MNRAS*, **356**, 1017
- Gallo, E., Fender, R. P., Miller-Jones, J. C. A., et al. 2006, *MNRAS*, **370**, 1351
- Gallo, E., Fender, R. P., & Pooley, G. G. 2003b, *MNRAS*, **344**, 60
- Gallo, E., Miller, B. P., & Fender, R. 2012, *MNRAS*, **423**, 590
- Garcia, M., Brown, W., Pahre, M., et al. 2000, *IAUC*, **7392**, 2
- Garcia, M. R., McClintock, J. E., Narayan, R., et al. 2001, *ApJL*, **553**, L47
- Gardner, E., & Done, C. 2012, *arXiv:1207.6984*
- Garmire, G. P., Bautz, M. W., Ford, P. G., Nousek, J. A., & Ricker, G. R., Jr. 2003, *Proc. SPIE*, **4851**, 28
- Gelino, D. M., Balman, Ş., Kızıloğlu, Ü., et al. 2006, *ApJ*, **642**, 438
- Gelino, D. M., Harrison, T. E., & Orosz, J. A. 2001, *AJ*, **122**, 2668
- Ghisellini, G., & Celotti, A. 2001, *A&A*, **379**, L1
- Gilfanov, M. 2010, *Lecture Notes in Physics* Vol. 794, ed. T. Belloni (Berlin: Springer-Verlag), **794** and **17**
- Greene, J., Bailyn, C. D., & Orosz, J. A. 2001, *ApJ*, **554**, 1290
- Grupe, D., Komossa, S., Leighly, K. M., & Page, K. L. 2010, *ApJS*, **187**, 64
- Gu, M., & Cao, X. 2009, *MNRAS*, **399**, 349
- Gültekin, K., Cackett, E. M., Miller, J. M., et al. 2012, *ApJ*, **749**, 129
- Hameury, J.-M., Barret, D., Lasota, J.-P., et al. 2003, *A&A*, **399**, 631
- Hameury, J.-M., Lasota, J.-P., McClintock, J. E., & Narayan, R. 1997, *ApJ*, **489**, 234
- Hawley, J. F., & Balbus, S. A. 2002, *ApJ*, **573**, 738
- Heinz, S. 2004, *MNRAS*, **355**, 835
- Heinz, S., & Sunyaev, R. A. 2003, *MNRAS*, **343**, L59
- Hjellming, R. M., Campbell-Wilson, D., & Hunstead, R. 1994, *IAUC*, **6055**, 1
- Ho, L. C. 2008, *ARA&A*, **46**, 475
- Homan, J., & Belloni, T. 2005, *Ap&SS*, **300**, 107
- Homan, J., Buxton, M., Markoff, S., et al. 2005, *ApJ*, **624**, 295
- Homan, J., Wijnands, R., Kong, A., et al. 2006, *MNRAS*, **366**, 235
- Houck, J. C., & Denicola, L. A. 2000, in *ASP Conf. Ser. 216, Astronomical Data Analysis Software and Systems IX*, ed. N. Manset, C. Veillet, & D. Crabtree (San Francisco, CA: ASP), **591**
- Hynes, R. I., Steeghs, D., Casares, J., Charles, P. A., & O'Brien, K. 2003, *ApJL*, **583**, L95
- Igumenshchev, I. V., Abramowicz, M. A., & Narayan, R. 2000, *ApJL*, **537**, L27
- Jain, R. K., Bailyn, C. D., Orosz, J. A., Remillard, R. A., & McClintock, J. E. 1999, *ApJL*, **517**, L131
- Jonker, P. G., Gallo, E., Dhawan, V., et al. 2004, *MNRAS*, **351**, 1359
- Jonker, P. G., Miller-Jones, J., Homan, J., et al. 2010, *MNRAS*, **401**, 1255
- Jonker, P. G., Miller-Jones, J. C. A., Homan, J., et al. 2012, *MNRAS*, **423**, 3308
- Jonker, P. G., & Nelemans, G. 2004, *MNRAS*, **354**, 355
- Kalemci, E., Tomsick, J. A., Buxton, M. M., et al. 2005, *ApJ*, **622**, 508
- Kennea, J. A., Romano, P., Mangano, V., et al. 2011, *ApJ*, **736**, 22
- Khargharia, J., Froning, C. S., Robinson, E. L., & Gelino, D. M. 2013, *AJ*, **145**, 21
- Kong, A. K. H., McClintock, J. E., Garcia, M. R., Murray, S. S., & Barret, D. 2002, *ApJ*, **570**, 277
- Körding, E., Rupen, M., Knigge, C., et al. 2008, *Sci*, **320**, 1318
- Kormendy, J., & Richstone, D. 1995, *ARA&A*, **33**, 581
- Kubota, A., & Makishima, K. 2004, *ApJ*, **601**, 428
- Kuulkers, E., Ibarra, A., Pollock, A., et al. 2010, *ATel*, **2912**, 1
- Lasota, J.-P., & Hameury, J.-M. 1998, in *AIP Conf. Ser. 431, Accretion Processes in Astrophysical Systems: Some Like It Hot!*, ed. S. S. Holt & T. R. Kallman (Melville, NY: AIP), **351**
- Laurent, P., Rodriguez, J., Wilms, J., et al. 2011, *Sci*, **332**, 438
- Livio, M., Ogilvie, G. I., & Pringle, J. E. 1999, *ApJ*, **512**, 100
- Maccarone, T. J. 2005, *MNRAS*, **360**, L30
- Maitra, D., & Bailyn, C. D. 2006, *ApJ*, **637**, 992
- Maitra, D., Markoff, S., Brocksopp, C., et al. 2009, *MNRAS*, **398**, 1638
- Malzac, J. 2007, *Ap&SS*, **311**, 149
- Malzac, J., Beloborodov, A. M., & Poutanen, J. 2001, *MNRAS*, **326**, 417
- Marconi, A., Risaliti, G., Gilli, R., et al. 2004, *MNRAS*, **351**, 169
- Markoff, S., Falcke, H., & Fender, R. 2001, *A&A*, **372**, L25
- Markoff, S., Nowak, M., Corbel, S., Fender, R., & Falcke, H. 2003, *A&A*, **397**, 645
- Markoff, S., Nowak, M. A., & Wilms, J. 2005, *ApJ*, **635**, 1203
- McClintock, J. E., Narayan, R., Garcia, M. R., et al. 2003, *ApJ*, **593**, 435
- McClintock, J. E., & Remillard, R. A. 1986, *ApJ*, **308**, 110
- McKinney, J. C., & Blandford, R. D. 2009, *MNRAS*, **394**, L126
- Meier, D. L., Koide, S., & Uchida, Y. 2001, *Sci*, **291**, 84
- Menou, K., Esin, A. A., Narayan, R., et al. 1999, *ApJ*, **520**, 276
- Merloni, A., & Fabian, A. C. 2002, *MNRAS*, **332**, 165
- Merloni, A., Heinz, S., & di Matteo, T. 2003, *MNRAS*, **345**, 1057
- Migliari, S., & Fender, R. P. 2006, *MNRAS*, **366**, 79
- Miller, J. M., Homan, J., Steeghs, D., et al. 2006a, *ApJ*, **653**, 525
- Miller, J. M., Pooley, G. G., Fabian, A. C., et al. 2012, *ApJ*, **757**, 11
- Miller, J. M., Raymond, J., Homan, J., et al. 2006b, *ApJ*, **646**, 394
- Miller-Jones, J. C. A., Gallo, E., Rupen, M. P., et al. 2008, *MNRAS*, **388**, 1751
- Miller-Jones, J. C. A., Jonker, P. G., Dhawan, V., et al. 2009, *ApJL*, **706**, L230
- Miller-Jones, J. C. A., Jonker, P. G., Maccarone, T. J., Nelemans, G., & Calvelo, D. E. 2011a, *ApJL*, **739**, L18
- Miller-Jones, J. C. A., Jonker, P. G., Ratti, E. M., et al. 2011b, *MNRAS*, **415**, 306
- Mirabel, I. F., Dhawan, V., Mignani, R. P., Rodrigues, I., & Guglielmetti, F. 2001, *Natur*, **413**, 139
- Mukai, K. 1993, *Legacy*, **3**, 21
- Nagar, N. M., Falcke, H., & Wilson, A. S. 2005, *A&A*, **435**, 521
- Narayan, R. 2005, *Ap&SS*, **300**, 177
- Narayan, R., Barret, D., & McClintock, J. E. 1997, *ApJ*, **482**, 448
- Narayan, R., Igumenshchev, I. V., & Abramowicz, M. A. 2000, *ApJ*, **539**, 798
- Narayan, R., & McClintock, J. E. 2008, *NewAR*, **51**, 733
- Narayan, R., McClintock, J. E., & Yi, I. 1996, *ApJ*, **457**, 821
- Narayan, R., & Yi, I. 1994, *ApJL*, **428**, L13
- Narayan, R., & Yi, I. 1995, *ApJ*, **444**, 231
- Nemmen, R. S., Storchi-Bergmann, T., Yuan, F., et al. 2006, *ApJ*, **643**, 652
- Nicastro, F. 2000, *ApJL*, **530**, L65
- Orosz, J. A., McClintock, J. E., Remillard, R. A., & Corbel, S. 2004, *ApJ*, **616**, 376
- Orosz, J. A., Steiner, J. F., McClintock, J. E., et al. 2011, *ApJ*, **730**, 75
- Paragi, Z., van der Horst, A. J., Granot, J., et al. 2010, *ATel*, **2906**, 1
- Pe'er, A., & Markoff, S. 2012, *ApJ*, **753**, 177
- Plotkin, R. M., Anderson, S. F., Brandt, W. N., et al. 2012a, *ApJL*, **745**, L27
- Plotkin, R. M., Markoff, S., Kelly, B. C., Körding, E., & Anderson, S. F. 2012b, *MNRAS*, **419**, 267
- Polko, P., Meier, D. L., & Markoff, S. 2013, *MNRAS*, **428**, 587
- Ptak, A., Terashima, Y., Ho, L. C., & Quataert, E. 2004, *ApJ*, **606**, 173
- Qiao, E., & Liu, B. F. 2013, *ApJ*, **764**, 2
- Quataert, E., Di Matteo, T., Narayan, R., & Ho, L. C. 1999, *ApJL*, **525**, L89
- Quataert, E., & Gruzinov, A. 2000, *ApJ*, **539**, 809
- Ratti, E. M., Jonker, P. G., Miller-Jones, J. C. A., et al. 2012, *MNRAS*, **423**, 2656
- Rees, M. J., Begelman, M. C., Blandford, R. D., & Phinney, E. S. 1982, *Natur*, **295**, 17
- Reis, R. C., Fabian, A. C., & Miller, J. M. 2010, *MNRAS*, **402**, 836
- Reis, R. C., Miller, J. M., Fabian, A. C., et al. 2011, *MNRAS*, **410**, 2497
- Remillard, R. A., & McClintock, J. E. 2006, *ARA&A*, **44**, 49

- Reynolds, M., & Miller, J. 2013, *ApJ*, **749**, 16
- Reynolds, M. T., & Miller, J. M. 2010, *ApJ*, **716**, 1431
- Reynolds, M. T., & Miller, J. M. 2011, *ApJL*, **734**, L17
- Russell, D. M., Fender, R. P., Hynes, R. I., et al. 2006, *MNRAS*, **371**, 1334
- Russell, D. M., Maitra, D., Dunn, R. J. H., & Markoff, S. 2010, *MNRAS*, **405**, 1759
- Russell, D. M., Markoff, S., Casella, P., et al. 2013, *MNRAS*, **429**, 815
- Rybicki, G. B., & Lightman, A. P. 1979, *Radiative Processes in Astrophysics* (New York: Wiley)
- Scaringi, S., K rding, E., Uttley, P., et al. 2012, *MNRAS*, **421**, 2854
- Shahbaz, T., Ringwald, F. A., Bunn, J. C., et al. 1994, *MNRAS*, **271**, L10
- Shapiro, S. L., & Teukolsky, S. A. 1983, *Black Holes, White Dwarfs, and Neutron Stars: The Physics of Compact Objects* (New York: Wiley)
- Shaposhnikov, N., Markwardt, C., Swank, J., & Krimm, H. 2010, *ApJ*, **723**, 1817
- Shemmer, O., Brandt, W. N., Netzer, H., Maiolino, R., & Kaspi, S. 2008, *ApJ*, **682**, 81
- Sikora, M., Stawarz, L., & Lasota, J.-P. 2007, *ApJ*, **658**, 815
- Sobolewska, M. A., Papadakis, I. E., Done, C., & Malzac, J. 2011, *MNRAS*, **417**, 280
- Soleri, P., Fender, R., Tudose, V., et al. 2010, *MNRAS*, **406**, 1471
- Soria, R., Fabbiano, G., Graham, A. W., et al. 2006, *ApJ*, **640**, 126
- Steehls, D., Miller, J. M., Kaplan, D., & Rupen, M. 2003, *ATel*, **146**, 1
- Steiner, J. F., McClintock, J. E., & Reid, M. J. 2012, *ApJL*, **745**, L7
- Stirling, A. M., Spencer, R. E., de la Force, C. J., et al. 2001, *MNRAS*, **327**, 1273
- Tomsick, J. A., Corbel, S., Fender, R., et al. 2003, *ApJ*, **582**, 933
- Tomsick, J. A., Corbel, S., & Kaaret, P. 2001, *ApJ*, **563**, 229
- Tomsick, J. A., Kalemci, E., & Kaaret, P. 2004, *ApJ*, **601**, 439
- Trump, J. R., Impey, C. D., Kelly, B. C., et al. 2011, *ApJ*, **733**, 60
- Uttley, P., Wilkinson, T., Cassatella, P., et al. 2011, *MNRAS*, **414**, L60
- Wilkinson, T., & Uttley, P. 2009, *MNRAS*, **397**, 666
- Winter, L. M., Mushotzky, R. F., Reynolds, C. S., & Tueller, J. 2009, *ApJ*, **690**, 1322
- Wu, Q., & Gu, M. 2008, *ApJ*, **682**, 212
- Xie, F.-G., & Yuan, F. 2012, *MNRAS*, **427**, 1580
- Yan, M., Sadeghpour, H. R., & Dalgarno, A. 1998, *ApJ*, **496**, 1044
- Younes, G., Porquet, D., Sabra, B., & Reeves, J. N. 2011, *A&A*, **530**, A149
- Yu, Z., Yuan, F., & Ho, L. C. 2011, *ApJ*, **726**, 87
- Yuan, F., & Cui, W. 2005, *ApJ*, **629**, 408
- Yuan, F., Taam, R. E., Misra, R., Wu, X.-B., & Xue, Y. 2007, *ApJ*, **658**, 282
- Zdziarski, A. A., Gierliński, M., Mikołajewska, J., et al. 2004, *MNRAS*, **351**, 791
- Zhang, W. M., Soria, R., Zhang, S. N., Swartz, D. A., & Liu, J. F. 2009, *ApJ*, **699**, 281